fluids

MDPI

Article

Boiling Phenomena and Heat Transfer Enhancement Effect on Micro/Nanoporous Sintered Copper Surfaces

Dong Ju Lee, Young Jae Yang, Dong-Wook Jerng * and Dong Eok Kim *

School of Energy System Engineering, Chung-Ang University, Seoul 06974, Republic of Korea; leedongju37@gmail.com (D.J.L.); yjkorea1318@cau.ac.kr (Y.J.Y.)
* Correspondence: dwjerng@cau.ac.kr (D.-W.J.); dekim@cau.ac.kr (D.E.K.)

Abstract

This study experimentally investigated boiling phenomena and heat transfer enhancement on sintered Cu micro/nanoporous surfaces under saturated pool boiling conditions. To evaluate the effects of the combined micro/nanostructures, microporous Cu layers and pillar-integrated surfaces were fabricated using micro-sized (diameter <75 mm) metal powder sintering, while nanostructures were formed through thermal oxidation. Boiling experiments revealed that the boiling heat transfer coefficient (BHTC) and critical heat flux (CHF) of the microporous Cu surfaces surpassed those of the reference surface SiO_2. The microporous pillar surface exhibited the best performance, demonstrating enhancements of approximately 2.7-fold and 7.3-fold in CHF and BHTC, respectively. High-speed imaging attributed this improvement to increased nucleation site density, rapid detachment and generation of small bubbles, efficient surface rewetting by capillary wicking, and liquid–vapor pathway separation enabled by the pillar geometry. Distinct transient temperature peaks and recoveries were observed on the oxidized pillar surfaces. Despite temporary overheating, strong capillary wicking from the superhydrophilic nanostructures recovered to the nucleate-boiling regime, which suppressed irreversible dryout and extended the boiling performance beyond the smooth surface CHF by 2.1 times. The results revealed that increasing the nucleation site density, enhancing the capillary-driven liquid supply, and ensuring effective separation of the vapor and liquid pathways improved the boiling heat transfer in multiscale porous structures. The sintered Cu micro/nanoporous surfaces demonstrated stable and efficient heat transfer across a wide range of heat fluxes, highlighting their potential for advanced thermal management applications and realizing optimally designed high-performance boiling surfaces.

Keywords: pool boiling; micro/nanostructure; critical heat flux; boiling heat transfer coefficient

check for updates

Academic Editor: D. Andrew S. Rees

Received: 22 September 2025
Revised: 31 October 2025
Accepted: 18 November 2025
Published: 20 November 2025

Citation: Lee, D.J.; Yang, Y.J.; Jerng, D.-W.; Kim, D.E. Boiling Phenomena and Heat Transfer Enhancement Effect on Micro/Nanoporous Sintered Copper Surfaces. *Fluids* **2025**, *10*, 303. https://doi.org/10.3390/fluids10110303

Copyright: © 2025 by the authors. Licensee MDPI, Basel, Switzerland. This article is an open access article distributed under the terms and conditions of the Creative Commons Attribution (CC BY) license (https://creativecommons.org/licenses/by/4.0/).

1. Introduction

Boiling heat transfer is one of the most effective heat dissipation modes in thermal management systems [1]. Owing to its high latent heat and ability to maintain small temperature differences between a heated surface and the working fluid, it is widely applied in various industries, including nuclear power reactors [2], thermal desalination plants [3], high-performance heat exchangers [4], and electronic device cooling [5]. In such applications, stable and efficient boiling ensures energy efficiency and maintains system reliability and safety. However, its performance is constrained by the critical heat flux (CHF). When the CHF is exceeded, vapor layer formation triggers a transition from nucleate to film boiling [6–8], which sharply increases the wall temperature. This is commonly

referred to as burnout or departure from nucleate boiling and potentially causes severe thermal failure.

While the CHF represents the upper safety limit of boiling heat transfer, the boiling heat transfer coefficient (BHTC) characterizes the effectiveness of heat transfer below this limit. A higher BHTC indicates the ability to transfer the same heat flux at a lower wall superheat, which indicates efficient bubble nucleation, growth, and departure. These bubble dynamics primarily enhance BHTC, thereby improving the overall thermal management performance. Consequently, studies have focused on enhancing both the CHF and BHTC to ensure safer and more efficient boiling heat transfer.

In recent years, various strategies have been investigated to improve the boiling performance [9–17] by modifying the surface morphology and wettability. Porous coatings have been employed to enhance the liquid supply to boiling surfaces through capillary wicking, thereby delaying local dryout. Finned and microchannel geometries [18,19] have been used to increase the effective surface area and remove vapor from the boiling surface. Gouda et al. [18] experimentally compared pool boiling on segmented finned and uniform microchannel surfaces with that on a plain Cu surface and observed a three-fold increase in the heat transfer coefficient for the segmented design.

Moreover, metallic foams [20–22] have been employed as boiling surfaces to provide continuous vapor escape pathways while simultaneously supplying liquid through their interconnected porous structures, thereby improving boiling performance. Lim et al. [21] investigated pool boiling on microthick metallic foam surfaces and reported notable enhancements in both the CHF and heat transfer coefficient, which were attributed to the highly permeable structure that facilitated efficient liquid–vapor transport.

Advanced surface structuring techniques such as laser patterning [23–26], chemical etching [27–29], metal powder sintering [30–36], and anodization [37] have been applied to further modulate surface wettability and increase the density of active nucleation sites. Wong et al. [26] investigated the saturated pool boiling of FC-72 on porous lattice structures fabricated by selective laser melting and observed notable improvements in the heat transfer and delayed CHF compared with a plain surface. Dang et al. [30] experimentally studied the saturated pool boiling of R245fa on Cu surfaces coated with sintered Cu powder layers, with and without nanostructure treatment. Both porous and nanotreated surfaces significantly enhanced the boiling heat transfer and CHF compared with those of a plain surface. In addition, the modified surfaces enabled earlier nucleation at the lower wall superheats and provided further improvement at low heat fluxes after nanotreatment.

Jun et al. [32] experimentally investigated the saturated pool boiling of water on Cu surfaces coated with sintered microporous layers and reported significant enhancements in both the nucleate boiling heat transfer and CHF compared with those of a plain Cu surface. These improvements were attributed to the random porous structures with reentrant-type cavities, and the performance was strongly influenced by the particle size and coating thickness. More broadly, such improvements are generally associated with enlarged surface areas, increased nucleation site densities, and capillary-driven liquid replenishment within porous or structured lattices.

Furthermore, significant improvements were achieved by ensuring efficient vapor escape paths [38,39] and promoting liquid replenishment through interconnected pores [40,41], thereby sustaining effective boiling heat transfer. Liu et al. [42] examined the pool boiling of FC-72 on micro/nanocomposite surfaces, where nanostructures were selectively formed on micropin fins. Surfaces with nanostructures at the micro-pin-fin tops exhibited earlier nucleation and significantly higher CHF and BHTC values than plain micro-pin-fin surfaces. Hybrid micro/nanostructured surfaces [42–44] have exhibited

synergistic effects, where microscale cavities stabilized bubble nucleation and nanoscale structures facilitated liquid spreading and rewetting of dried regions.

Additionally, nanofluid-based approaches have been investigated to enhance boiling performance [45–48]. These studies demonstrated that nanoparticle deposition during boiling can increase the CHF and promote nucleation by modifying surface wettability and roughness, while also improving liquid spreading through induced capillary effects. However, such improvements often depend on particle concentration, boiling duration, and surface deposition history, leading to inconsistencies in reproducibility and long-term stability. Moreover, practical challenges such as particle agglomeration and surface fouling limit their applicability in systems requiring clean and stable operation.

In contrast, surface modification offers stable and repeatable enhancement of CHF and BHTC through geometrically defined multiscale structures that promote efficient liquid vapor pathway separation and capillary wicking without altering the working fluid.

Most recently, various design strategies to further enhance boiling performance, including additively manufactured microchannels and chimneys for effective liquid vapor pathway control [49], multilayer-gradient-porosity pillars that balance nucleation and liquid replenishment [50], and micro/nanocomposite porous structures that regulate vapor motion frequency and liquid film behavior [51]. Thermal plasma-sprayed coatings [52] and 3D-printed thermal enhancement surfaces [53] have also demonstrated scalable fabrication routes and geometric optimization for high heat flux dissipation. These studies have collectively advanced the understanding of multiscale heat transfer enhancement through structural design, wettability control, and capillary wicking.

Although numerous studies have addressed boiling enhancement by surface modification, most have focused on limited structural coupling or partial scale integration. In contrast, the present study examines a fully hierarchical architecture combining milli-, micro-, and nanoscale features to clarify their coupled effects on boiling behavior. The hierarchical structure is composed of microporous networks and pillar geometry forms coupled with micro-millimeter scale pathways that enable efficient liquid supply and vapor removal, thereby maintaining stable boiling at high heat fluxes.

The present work is based on the experimental setup and data reported in our previous study [54], providing an extended analysis from a new perspective to elucidate the boiling behavior on micro/nanostructured porous surfaces. In particular, the present study conducts a more detailed analysis of bubble dynamics and transient thermal behavior to clarify the underlying boiling mechanisms.

In this study, microporous Cu surfaces were fabricated by powder sintering, and additional nanoscale oxide structures were fabricated via thermal oxidation under atmospheric conditions. Additionally, pool boiling experiments were performed to identify the key factors influencing boiling enhancement. The findings from this study provide a deeper understanding of the boiling mechanisms and offer insights into optimizing multiscale porous surfaces to achieve stable and efficient heat transfer over a wide range of heat fluxes.

2. Experiments

2.1. Pool Boiling Experimental Setup

In this study, a pool boiling experimental setup was established to investigate the boiling heat transfer characteristics and phenomena of micro/nanoporous sintered Cu surfaces. Each boiling experiment was performed under saturated conditions at atmospheric pressure (100 °C). The experimental setup and test specimen were configured as shown in Figure 1. Deionized water (DAEJUNG Chemicals & Metals, Siheung, Republic of Korea) was used as the working fluid and heated using a 1 kW cartridge heater placed inside

the boiling chamber. When the water reached saturation temperature, it was held for an additional 30 min to remove the dissolved non-condensable gases.

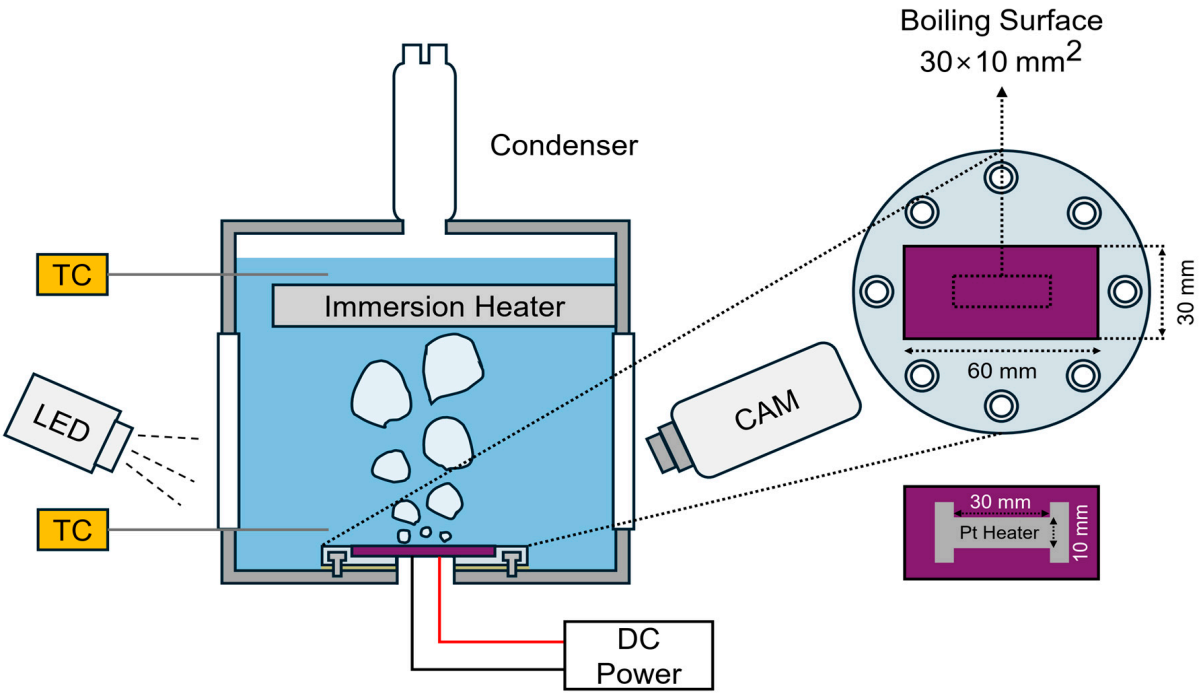


Figure 1. Pool boiling experimental setup and boiling substrate configuration.

The bulk-liquid temperature was monitored using two K-type thermocouples positioned at the top and bottom of the chamber. The signal from the lower thermocouple was processed using a proportional–integral–derivative temperature controller (TZ4ST-24C, Autonics, Pusan, Republic of Korea), which relayed the control output to a thyristor power regulator (TPR-2N220V25AMR, Hanyoung Nux, Incheon, Republic of Korea). The regulator controlled the electrical power supplied to the cartridge heater, thereby maintaining the saturation temperature during the experiment.

The substrates were fabricated from silicon wafers (60 × 30 mm^2, thickness: 525 mm) thermally grown with a SiO_2 layer (thickness: 500 nm) serving as an electrical insulating layer. Subsequently, each wafer specimen was securely mounted on a polycarbonate holder using epoxy bonding, and the boiling chamber was sealed to prevent water leakage. For surface heating, Joule heating was applied using a platinum (Pt) thin-film heater (30 × 10 mm^2, thickness: 120 nm) deposited on the back side of the boiling surface by e-beam evaporation. The Pt electrodes were soldered and connected to a DC power supply (PSW 80V-40A, GWINSTEK, New Taipei city, Taiwan), which was operated in the constant voltage mode to regulate the applied surface heat flux.

The surface temperature was determined from the linear relationship between the resistance of Pt and temperature. Before each experiment, this linear calibration curve was established at four reference points (60, 80, 100, and 120 °C) in a forced convection oven (OF-01E, JeioTech, Daejeon, Republic of Korea) using a four-wire Ohm measurement method (DAQ970A, Keysight). The calibration curve exhibited excellent linearity ($R^2 > 0.999$) (Figure 2).

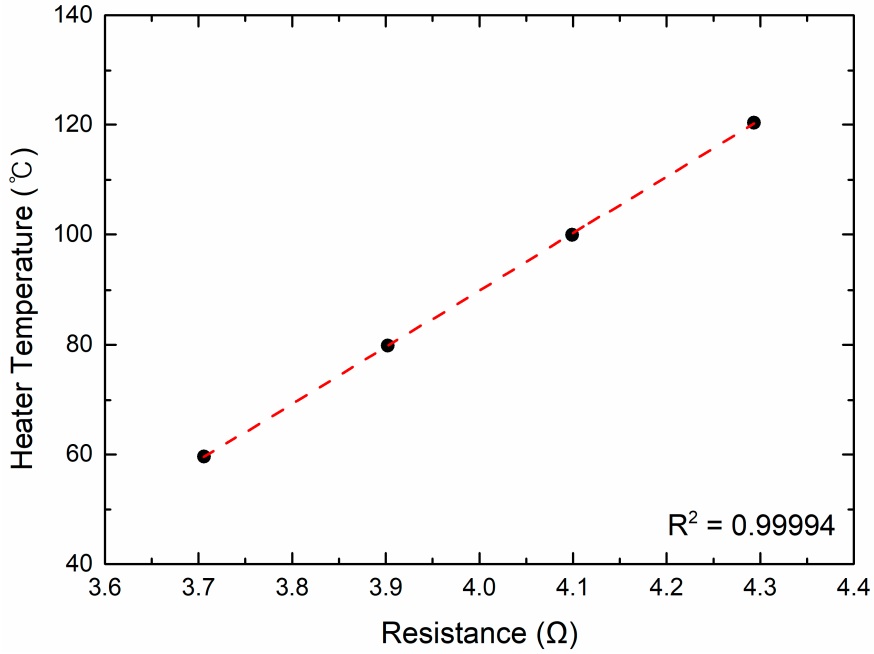


Figure 2. Relationship between the resistance and temperature of the Pt heater.

Most steady-state boiling conditions in this study were within this calibrated range, although a few data points during high heat-flux operation and transient superheat events reached surface temperatures up to approximately 210 °C. The validity of the linear approximation in this temperature region was confirmed based on the findings of Liu et al. [55], who demonstrated that a thin Pt film (thickness ≈ 100 nm) maintains stable linear R–T characteristics up to about 230 °C, ensuring sufficient accuracy for analyzing both steady-state and transient superheat behavior. Moreover, recent work on Pt thin-film RTDs by Wang et al. [56] has further shown excellent linear R–T correlation across 25–1000 °C and demonstrated outstanding long-term stability under repeated thermal cycling, confirming that Pt films preserve their linear resistive behavior even at temperatures far exceeding the range analyzed in this study.

During the boiling experiments, the voltage (V) and current (I) were measured using voltage (MT4Y-DV-43, Autonics, Pusan, Republic of Korea) and current (MCR-S-10-50-UI-SW-DCI, Phoenix Contact, Blomberg, Germany) meters, respectively. The Pt heater resistance (R_{Pt}) was calculated using Ohm's law ($V = IR_{Pt}$), and the surface heat flux (q_s) was obtained using $q_s = VI/A_s$, where A_s is the boiling surface area (30 × 10 mm^2), identical to the Pt heater area shown in Figure 1. It was assumed that all heat generated by the Pt heater was transferred to the boiling surface.

However, since heat conduction from the Pt heater actually occurs laterally through the silicon wafer, we calculated this heat loss effect to examine the validity of this assumption. Based on calculations referenced to the SiO_2 surface, when the surface heat flux exceeds 300 kW/m^2, more than 95% of the generated heat is conserved within the defined boiling surface, and this fraction converges to over 98% at heat fluxes above 800 kW/m^2. Therefore, this definition of boiling surface area is considered reasonable for this experimental configuration used in this study.

The heat transfer between the Pt heater and the boiling surface through the Si wafer was assumed to occur by one-dimensional conduction through the Si wafer and thin layers. The surface heat flux and temperature of the Pt film (T_{Pt}) were used to calculate the temperature of the boiling surface as $T_s = T_{Pt} - q_s \sum \delta_i / k_i$, where δ_{Si} = 524 μm, δ_{SiO_2} = 2 × 500 nm, δ_{Cu} = 2 μm, k_{Si} = 100 W/mK, k_{SiO_2} = 0.8 W/mK and k_{Cu} = 400 W/mK.

The thermal conductivity of silicon (k_{Si}) was assumed to be 100 W/mK in this study. This value was determined based on the experimental data reported by Yamasue et al. [57], in which the thermal conductivity of solid silicon decreases with increasing temperature, from approximately 140 W/mK at 20 °C to 80 W/mK at 200 °C. Given that the surface temperature in this experiment mainly ranged from 100 to 130 °C, corresponding to a thermal conductivity of silicon of about 100 W/mK, the use of this representative value is considered appropriate for the present study.

The experimental data were recorded using a data acquisition system (DAQ970A, Keysight, Santa Rosa, CA, USA). The boiling phenomena were visualized using a high-speed camera (Miro M310, Phantom, Wayne, MI, USA) at a frame rate of 1000 fps and illuminated by a 120 W white light LED source.

2.2. Surface Characteristics of Tested Substrates

Based on the reference surface SiO_2, four types of microporous surfaces were fabricated, and their characteristics are summarized in Table 1. Microporous structures were prepared using metal powder sintering. A Cu thin layer (thickness: 2 μm) with a Ti adhesion layer (thickness: 20 nm) was first deposited on the wafer surface using sputtering to allow subsequent Cu particle sintering.

Table 1. Details of the fabricated boiling surfaces.

Surface	Composition	Fabrication Process
SiO_2	SiO_2, 500 nm	Thermal oxidation of Si wafer
Cu-1L	Microporous Cu layer, thickness ≈ 70 mm	Powder sintering
Cu-Pil	Microporous Cu layer with pillars	Powder sintering
CuO-1L	Oxidized microporous Cu layer	Powder sintering + thermal oxidation
CuO-Pil	Oxidized microporous Cu layer with pillars	Powder sintering + thermal oxidation

To fabricate Cu-1L and Cu-Pil, spherical Cu particles (diameter <75 mm, 99.9% purity, Avention) were placed in a graphite mold and sintered onto a thin Cu layer at 850 °C for 1 h in a vacuum furnace (SH-FU-1.5MGV, SAMHEUNG, Sejong, Republic of Korea) under an Ar atmosphere. The chamber pressure was maintained slightly above atmospheric pressure to prevent contamination from ambient air. To fabricate nanostructures on microporous surfaces, Cu-1L and Cu-Pil were subjected to thermal oxidation [58] in a muffle furnace (SH-FU-27MG, SAMHEUNG) at 600 °C for 30 min under atmospheric conditions, producing nanoscale oxide structures denoted as CuO-1L and CuO-Pil.

The diameter, height, and center-to-center pitch of the cylindrical pillars in Cu-Pil and CuO-Pil were 2 mm, 1 mm, and 2.6 mm, respectively. Before the experiments, all substrates were cleaned in an ultrasonic chamber using acetone (>99.8%, DAEJUNG Chemicals & Metals, Siheung, Republic of Korea), isopropyl alcohol (>99.7%, DAEJUNG Chemicals & Metals, Siheung, Republic of Korea), and deionized water for 20 min each. Figure 3 shows the pictures of boiling substrates and the dimension of pillar structure.

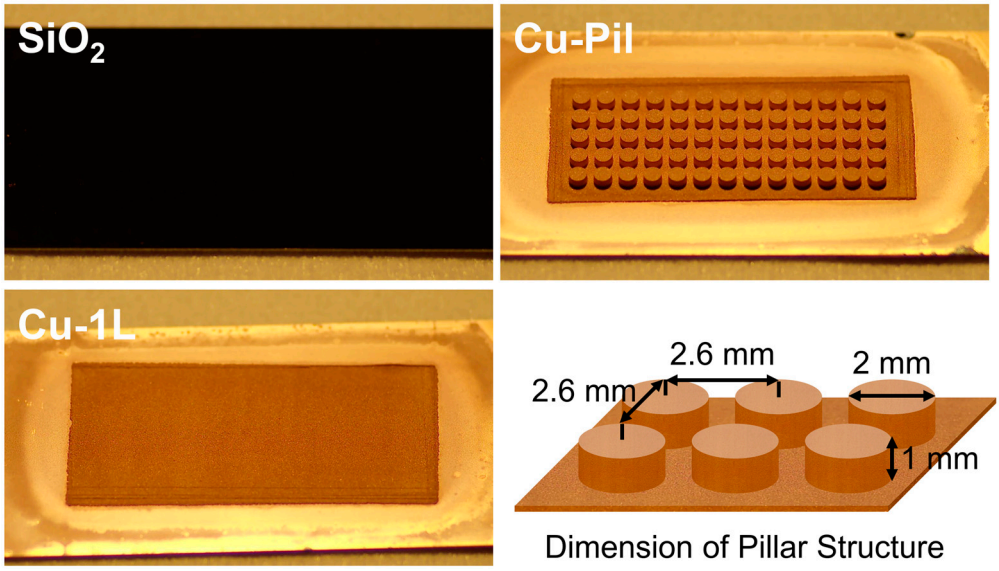


Figure 3. Images of the boiling substrates and details of the pillar structure.

2.3. Characterization of the Tested Substrates

Figure 4 shows the images used for static contact angle (CA, θ_s) measurement. To evaluate the wettabilities of the fabricated substrates, a sessile water drop (10 mL) was placed on each surface and imaged using a CMOS camera (TrueChrome Metrics, Tucsen, Fuzhou, China). The CA was determined using a CA measurement plugin integrated into the ImageJ 1.54g software (ImageJ 1.54g, NIH). The CA of SiO_2 was measured as 72.0°. However, for the microporous surfaces (Cu-1L, Cu-Pil, CuO-1L, and CuO-Pil), the water droplet immediately spread into the microporous structures instead of forming a stable sessile drop, resulting in an apparent CA of 0°. This behavior arises from strong capillary wicking, in which pores rapidly draw liquid into the structure. This spontaneous penetration indicates the superior wettability of the microporous surfaces.

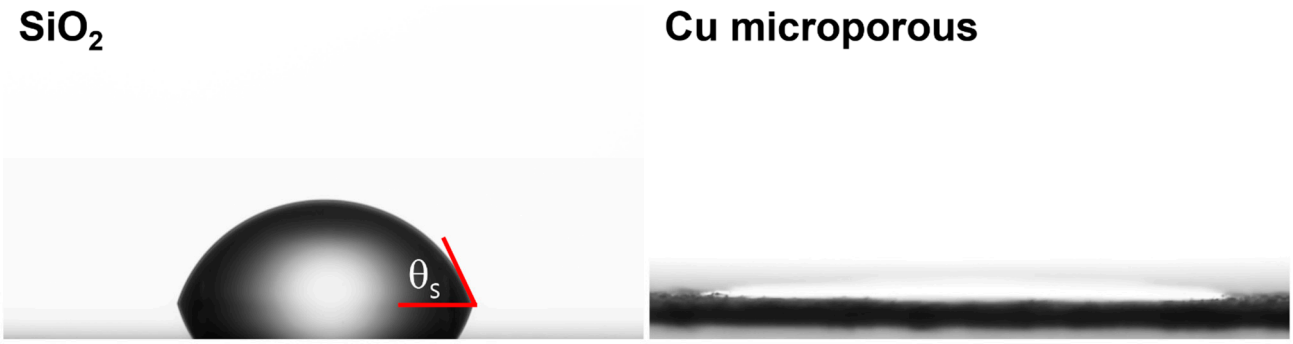


Figure 4. Measurement of the contact angle.

To further clarify the limitation of describing surface characteristics by the apparent contact angle, a droplet spreading test was conducted to visualize and quantify the capillary wicking behavior. A deionized water droplet was dropped on the Cu-1L and CuO-1L surfaces, and the spreading process was recorded using a high-speed camera at 1000 fps. The sequential images in Figure 5 and the time-dependent variation in wetted area and spreading velocity in Figure 6 clearly show that the CuO-1L surface exhibited faster lateral spreading and stronger capillary wicking compared to the Cu-1L surface.

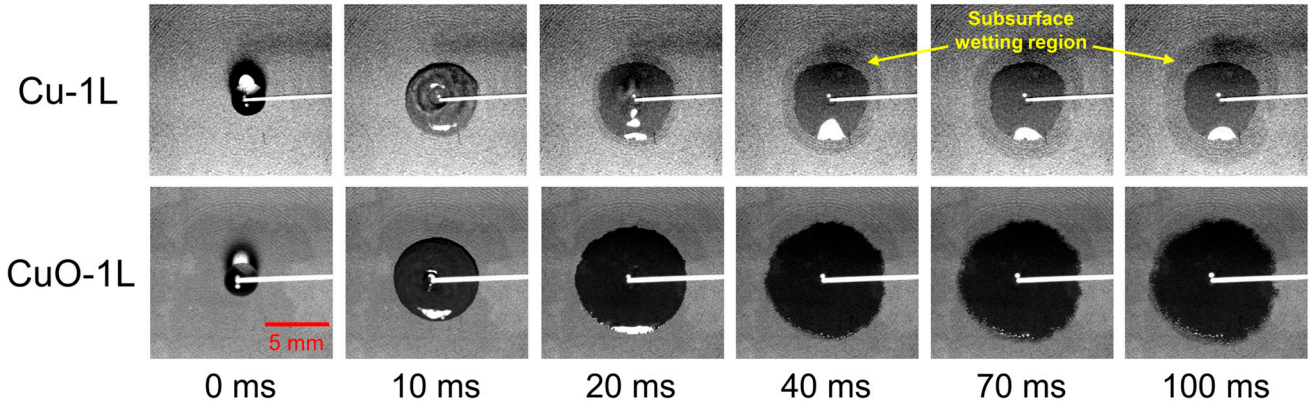


Figure 5. Sequential images of droplet spreading dynamics on Cu-1L and CuO-1L surfaces.

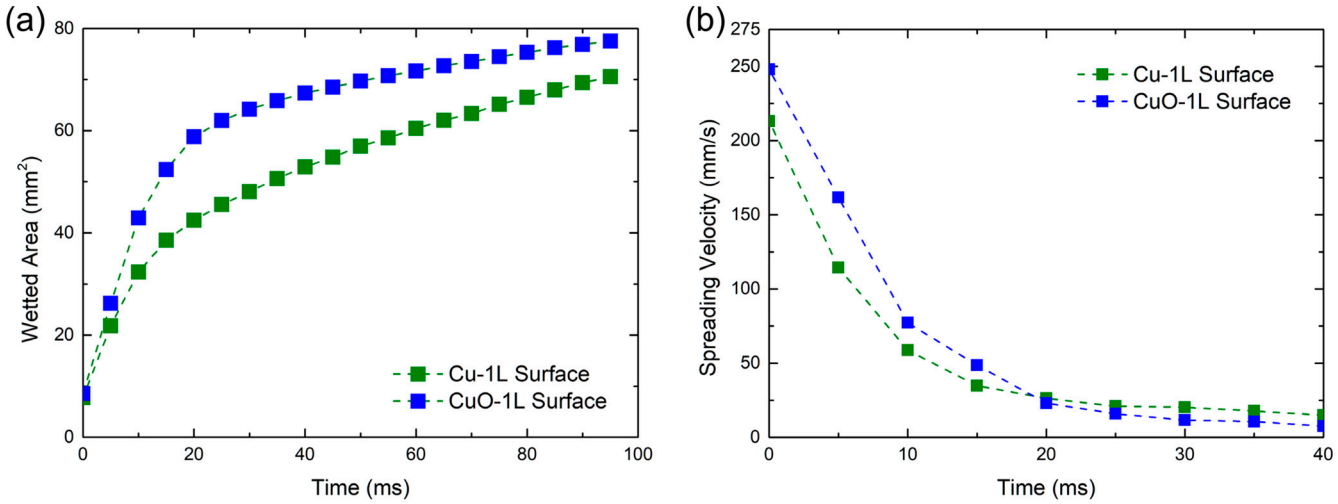


Figure 6. Temporal variation in (**a**) wetted area and (**b**) spreading velocity on Cu-1L and CuO-1L surfaces.

The CuO-1L surface displayed a higher spreading velocity and larger wetted area during the initial stage (<20 ms). However, beyond 20 ms, its spreading velocity gradually decreased and became comparable to that of the Cu-1L surface. At this stage, the visible droplet on the Cu-1L surface no longer expanded laterally, while the wetted area within the porous network continued to increase, indicating liquid absorption into the porous structure due to strong internal wicking. In contrast, the CuO-1L surface maintained pronounced wicking near the surface–liquid interface above the porous structure, allowing the droplet to continue expanding for a longer duration. These observations were used to characterize the spreading kinetics and to compare the dominant liquid transport mechanisms between the two surfaces.

As shown in Figure 7a,b, the boiling surfaces were photographed using a field-emission scanning electron microscope (FE-SEM). The images reveal well-formed microporous structures and nanostructures. These images were processed to analyze the pore size distribution, yielding the results shown in Figure 7c. The ratios of the pore area to the total area were 7.77% and 2.96% in Cu-1L and CuO-1L, respectively. They all ranged in several square micrometers. Pores with an area smaller than 10 μm^2 accounted for 36.61% and 59.62% of the total area on Cu-1L and CuO-1L, respectively. Thus, the CuO-1L surface contained a greater proportion of smaller cavities, suggesting that thermal oxidation promoted the formation of close-ended pores, which served as additional nucleation sites.

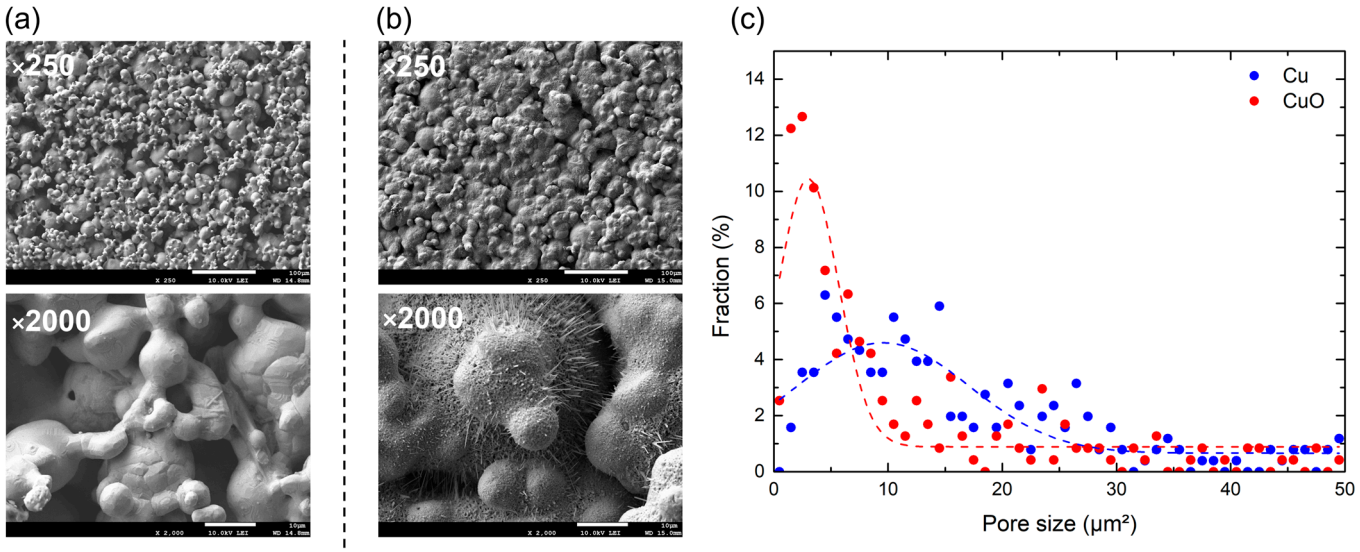


Figure 7. FE-SEM images (×250, ×2000) of (**a**) Cu-1L and (**b**) CuO-1L. (**c**) Plot of the pore size distribution.

In addition, the dimensions of the nanostructures were quantified (Figure 8). Their lengths were 0.5–5 μm with widths below 1 μm, forming needle-like morphologies with high aspect ratios. These nanoscale features enhanced surface wettability, which facilitated capillary-driven liquid spreading, efficient surface rewetting, and improved boiling heat transfer.

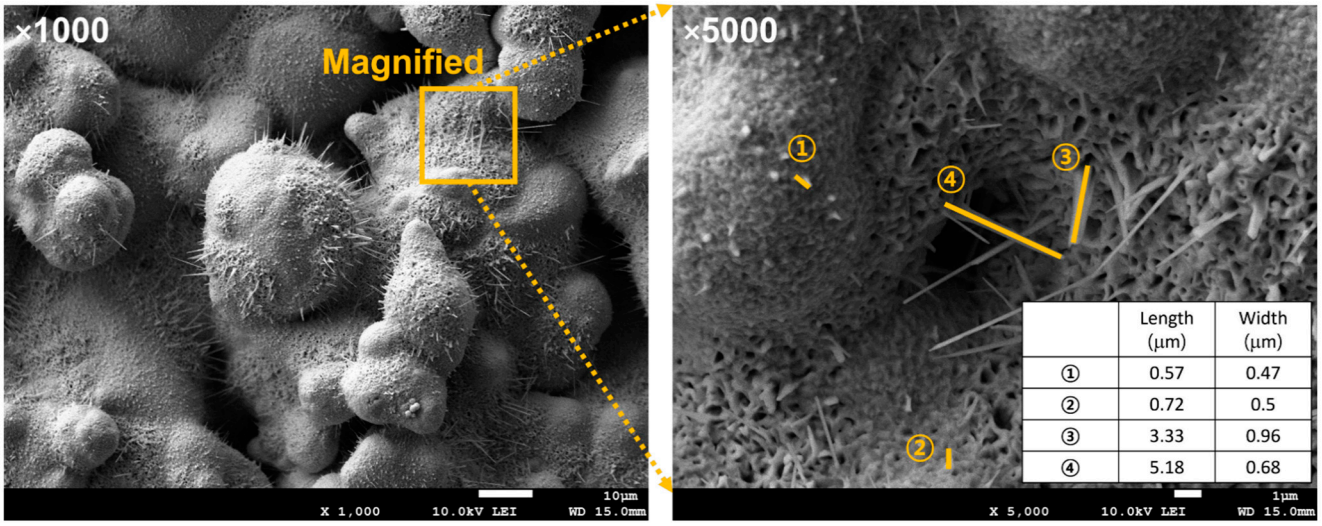


Figure 8. FE-SEM image and dimensions of nanoscale oxide structures.

2.4. Uncertainty Analysis

The experimental uncertainties were calculated using the method suggested by Kline [59] and referenced by Moffat [60]:

$$U_R = \sqrt{\sum_{i=1}^{n} \left(\frac{\partial R}{\partial x_i} u_{x_i} \right)^2}, \quad (1)$$

where U_R, R, x_i, and u_{x_i} denote the absolute uncertainty, the calculated results from the independent variable, the dependent variable, and the corresponding uncertainties of x_i, respectively.

The experimental uncertainty analysis in this study estimates the uncertainty values of power, heat flux (q_s), wall superheat temperature ($\Delta T_{sup} = T_w - T_{sat}$) and BHTC

($h = q_s/\Delta T_{sup}$). The measurement uncertainties were estimated based on the instrument specifications provided in the datasheets. The uncertainties of voltage and current were taken as ±0.5 V and ±0.05 A, respectively, and the Type K thermocouple uncertainty was assumed to be ±1 °C. Table 2 shows these results.

Table 2. Absolute and relative uncertainties of parameters.

	Absolute Uncertainty		Relative Uncertainty	
	Value	**Unit**	**Value**	**Unit**
Power	0.68–7.48	W	0.91–9.27	%
Surface heat Flux (q_s)	2.27–24.92	kW/m^2	0.91–9.27	%
Wall superheat (ΔT_{sup})	1.00–1.01	°C	3.29–64.17	%
BHTC (h)	0.19–95.82	kW/m^{2}K	3.44–34.24	%

To further evaluate the influence of these uncertainties on the calculated parameters, the relative uncertainties of q_s and h were plotted as a function of heat flux, as shown in Figure 9a,b. The surface exhibiting the maximum overall uncertainty was selected as a representative reference for this analysis to provide a conservative evaluation. Although several data points at very low wall superheats or low heat fluxes exhibited relatively higher uncertainty, the overall trend showed a gradual decrease in uncertainty with increasing heat flux, despite minor local fluctuations. These localized variations did not alter the general trend or interpretation of the experimental results, confirming that the experimental data are sufficiently reliable for analyzing boiling performance.

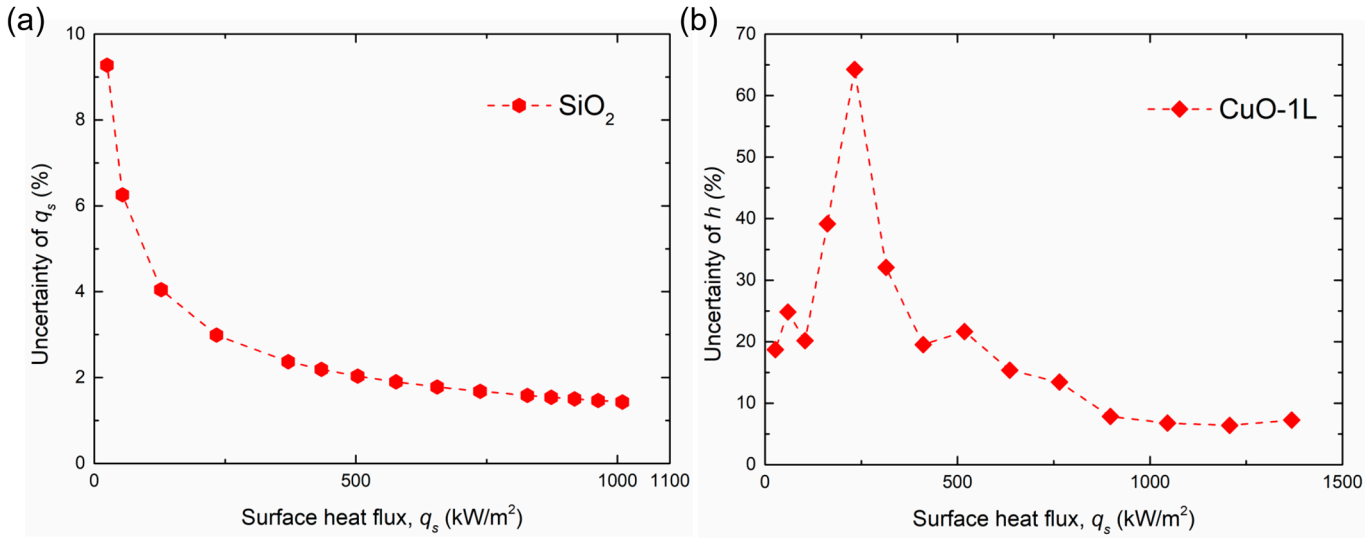


Figure 9. Variation in relative uncertainties in (**a**) surface heat flux (q_s) and (**b**) BHTC (h) with heat flux.

3. Results and Discussion

Figure 10a shows the experimental pool boiling curves obtained in this study. The CHF values were significantly enhanced for all the microporous surfaces. In particular, the Cu-Pil surface exhibited the highest CHF of 2746 kW/m^2, which was approximately 2.7 times higher than that of the SiO_2 surface. Moreover, the Cu-Pil surface achieved the highest BHTC of 381.2 kW/m^{2}K, which was approximately 7.3 times greater than that of SiO_2.

For the smooth SiO_2 surface, the wall superheat temperature increased with the surface heat flux, which was consistent with the general trend of conventional pool boiling curves

reported. However, on the microporous surfaces, the wall superheat temperature decreased as the heat flux increased to approximately 250 kW/m^2. This behavior is attributed to enhanced capillary wicking and liquid replenishment within the porous structures after the onset of nucleate boiling (ONB), which improves surface rewetting and reduces the wall temperature despite increasing heat flux. This inversion in the wall superheat temperature has been recently reported [61].

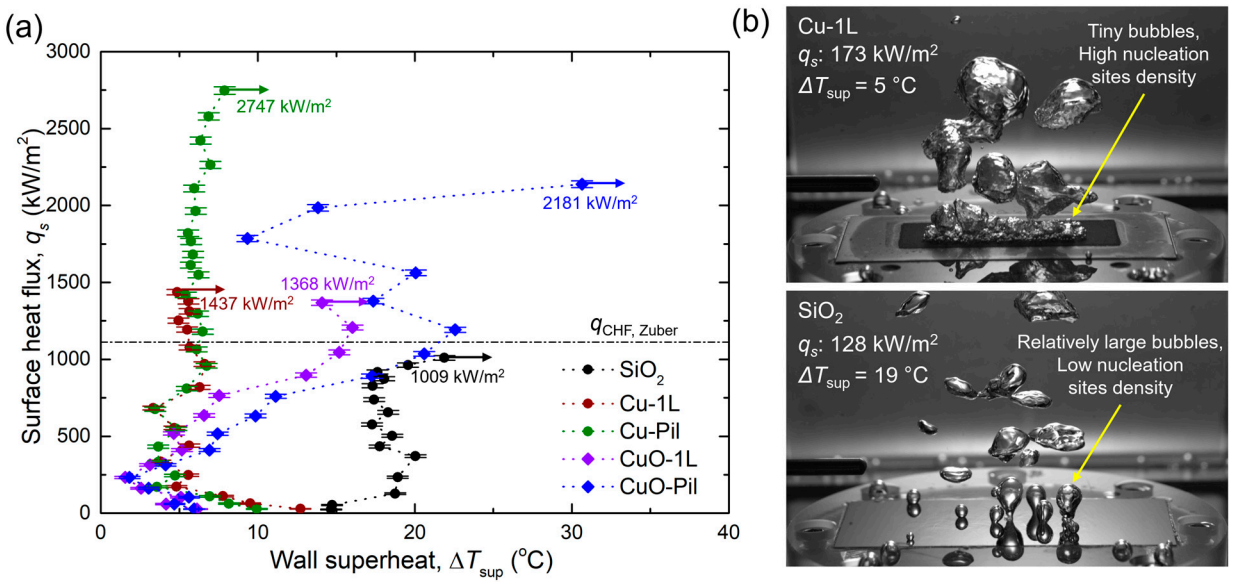


Figure 10. (**a**) Experimental pool boiling curves of the tested boiling surfaces [62]. (**b**) Differences in the bubble behavior of microporous and smooth surfaces.

Furthermore, the boiling heat transfer tendency depended on the material properties. As the surface heat flux increased, the wall superheat and CHF of surfaces comprising the same porous structure (Cu-1L with Cu-Pil and CuO-1L with CuO-Pil) exhibited gradually diverging trends (Figure 10). However, the wall superheat and BHTC of each group exhibited similar shape variations at low surface heat fluxes (q_s < 400 kW/m^2) (Figure 11).

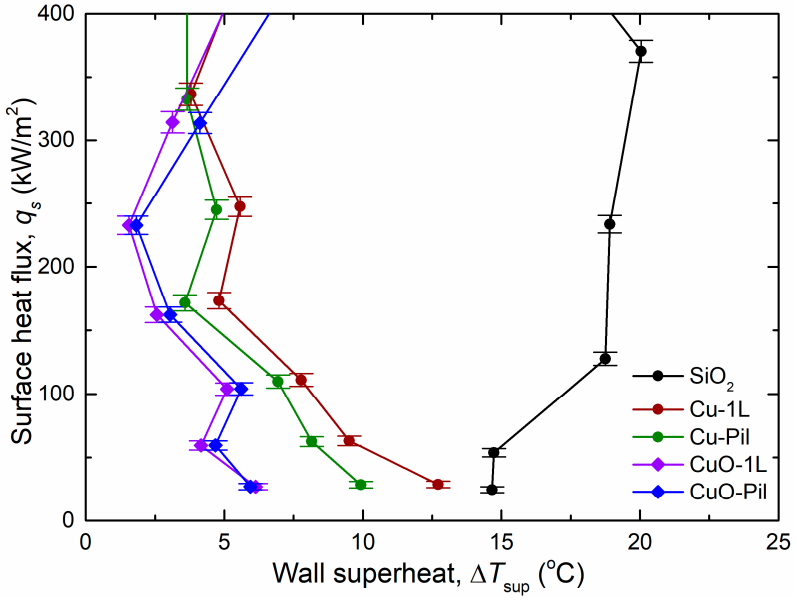


Figure 11. Boiling curves at low surface heat flux (q_s < 400 kW/m^2).

Therefore, among the surfaces of the same material and microporous structure, the boiling characteristics were strongly influenced by the nucleation site density and its material properties rather than by its millimeter-scale structure at low surface heat flux conditions.

Distinct differences in bubble dynamics were observed between the microporous and smooth surfaces (Figure 10b). On the microporous surfaces, numerous small bubbles nucleated and detached continuously, whereas the smooth surface produced only a few large bubbles and exhibited a considerably higher surface temperature. These results indicate that microporous surfaces provide a higher density of active nucleation sites, facilitating frequent bubble generation and departure, thereby enhancing the boiling heat transfer. Furthermore, the superior wettability of the microporous surfaces promoted efficient liquid replenishment by capillary wicking after bubble departure, suppressing local dryout, and thereby maintaining a relatively low surface temperature.

In Figure 10a, the correlation proposed by Zuber [62] (Equation (2)) was used to estimate the theoretical CHF.

$$q''_{CHF,Zuber} = 0.131 h_{lv} \rho_v \left[\frac{\sigma g (\rho_l \ \rho_v)}{\rho_v^2} \right]^{0.25}, \quad (2)$$

where h_{lv}, ρ_v, ρ_l, σ and g denote the latent heat of vaporization, vapor density, liquid density, surface tension, and gravitational acceleration, respectively. The experimental value of CHF for SiO_2 was consistent with Zuber's correlation, which confirmed the reliability of the experimental setup and measurement procedures.

To further clarify the magnitude of CHF enhancement relative to the theoretical hydrodynamic limit, the experimental CHF values were normalized using Zuber's correlation for the smooth surface under the same pressure and fluid conditions. As shown in Figure 12, the smooth SiO_2 surface exhibited a CHF ratio close to unity, whereas the multiscale porous and pillar structure surfaces demonstrated significantly higher normalized CHF values, reaching up to approximately 2.5 times Zuber's prediction.

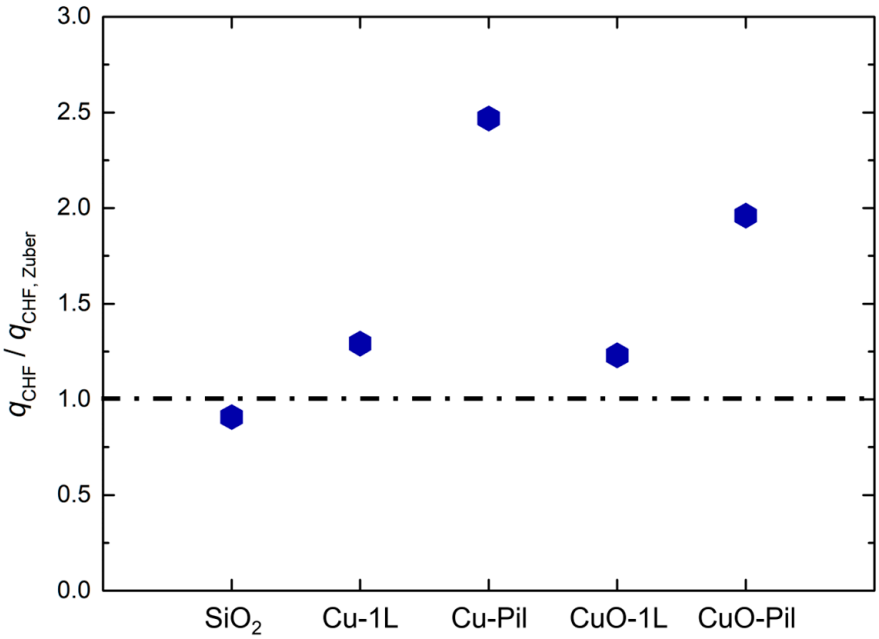


Figure 12. Normalized CHF ratio based on Zuber's correlation [61].

This result suggests that the CHF no longer follows a purely hydrodynamic instability limit. Instead, it is increasingly governed by capillary liquid supply through wicking,

indicating a partial shift in the dominant limiting mechanism. In other words, the hydrodynamic limit was effectively overcome by enhanced liquid replenishment enabled by the multiscale porous structure.

Distinct bubble dynamics were observed between the smooth SiO_2 surface and the microporous surfaces at ONB (Figure 13). While the SiO_2 surface exhibited only a few large bubbles, the microporous surfaces generated numerous tiny bubbles owing to their much higher nucleation site density, leading to reduced wall superheating and enhanced BHTC (Figure 14a) under low heat flux conditions. Moreover, among the microporous surfaces, CuO produced a greater number of smaller bubbles than the Cu surfaces, suggesting that thermal oxidation further increased the density of active nucleation sites.

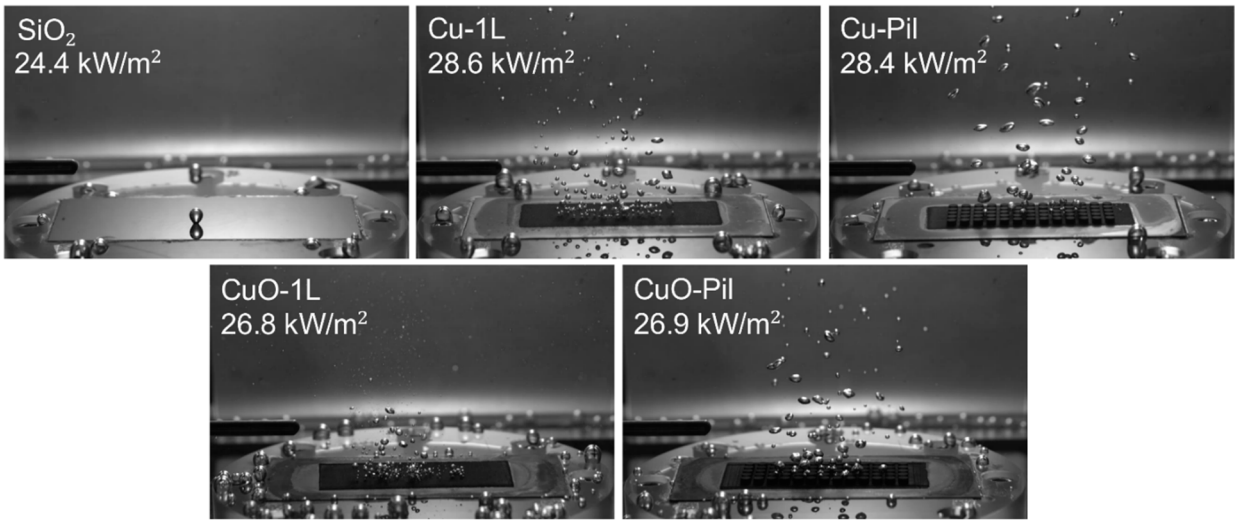


Figure 13. Bubble behavior at ONB.

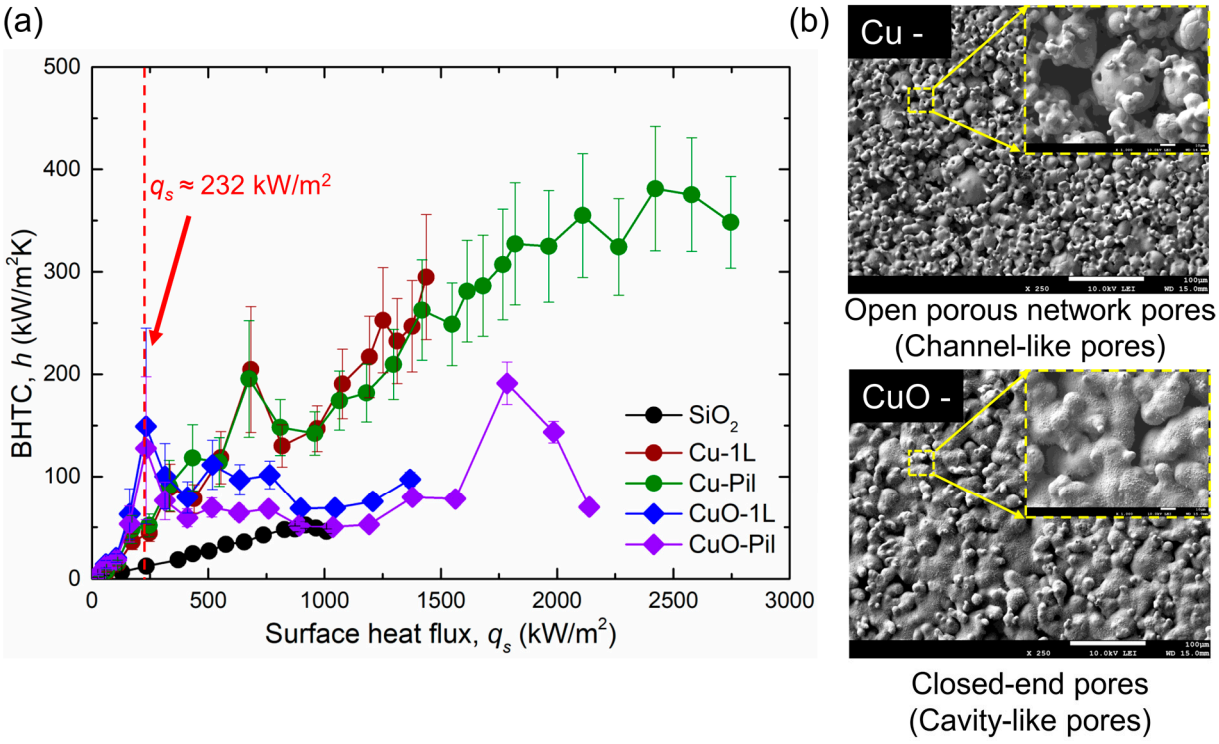


Figure 14. (**a**) Variations in BHTC with surface heat flux for the five tested surfaces and (**b**) SEM images of the microporous and oxidized micro/nano surfaces.

Consequently, the CuO surfaces exhibited higher BHTC and lower wall superheat than the Cu surfaces at low surface heat flux. The reduction in wall superheat after ONB was more pronounced in the pool boiling curve (Figure 11), owing to variations in the pore morphology. The microporous Cu surface contained open porous-network pores inside the structure, whereas the thermally oxidized CuO surface developed closed-end cavity-like pores, which altered the bubble dynamics and sustained efficient boiling heat transfer at a low surface heat flux (Figure 14b).

To quantitatively validate these observations, the nucleation site density (NSD), bubble departure diameter, and frequency were analyzed using high-speed visualizations (1000 fps). Figure 15a shows that the oxidized and hierarchically structured surfaces (CuO-1L, CuO-Pil) exhibited markedly higher NSD values compared with the non-oxidized ones (Cu-1L, Cu-Pil) and the smooth SiO_2 surface. The Cu-1L surface presented the maximum NSD, approximately 105 times greater than that of SiO_2, demonstrating the abundance of active nucleation sites provided by the porous microstructure.

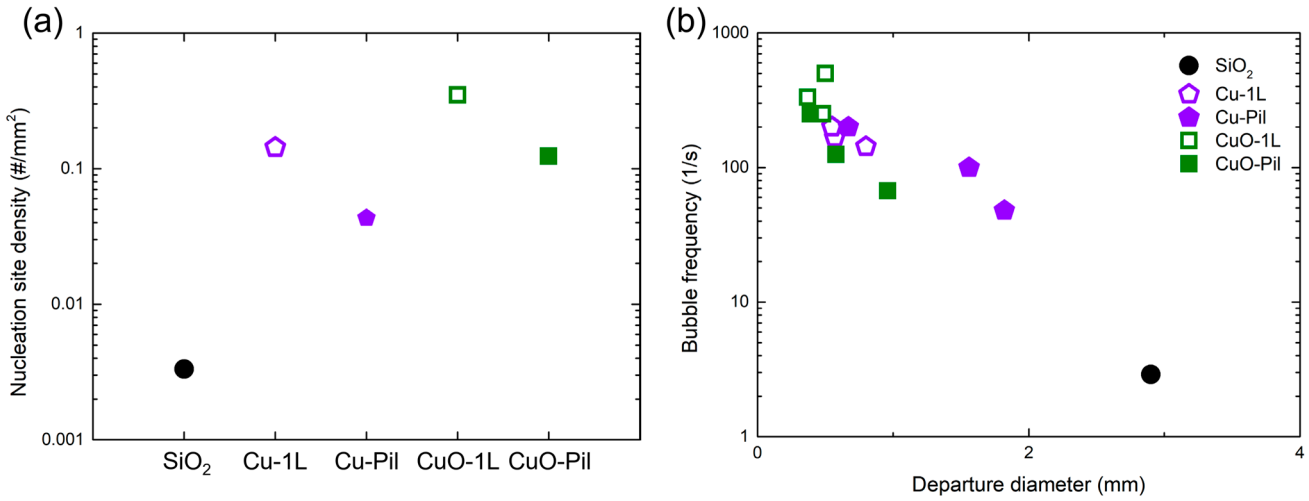


Figure 15. (**a**) Nucleation site densities and (**b**) bubble frequency with departure diameter of examined surfaces at ONB ($q_s \approx 30$ kW/m^2).

Figure 15b demonstrates that the microporous surfaces exhibited smaller bubble departure diameters and much higher bubble frequencies than the smooth SiO_2 surface, confirming the rapid bubble renewal process on porous structures. In particular, the CuO-1L surface showed the highest frequency (≈500 Hz), about 170 times greater than that of SiO_2. These results quantitatively substantiate the visual observations and highlight that the distinct pore morphologies of the Cu and CuO surfaces govern bubble dynamics, which underlie their superior boiling performance.

The SEM images showed that the Cu surface possessed an open porous network of pores inside the surface structure, which facilitated liquid transport, whereas the CuO surface consisted of closed-end pores that primarily served as nucleation cavities. These morphological differences generated a higher density of nucleation sites and more frequent bubble departures on the CuO surface at low heat fluxes, resulting in an enhanced BHTC compared with that of the Cu surface.

Nevertheless, the BHTC of the CuO surface reached its maximum value and subsequently decreased (red mark in Figure 14a), whereas that of the Cu surface continued to increase. This reduction on the CuO surface is attributed to the insufficient liquid supply caused by the isolated pore configuration. As the surface heat flux increased, the benefit of the enhanced heat transfer from the higher nucleation site density diminished, and the ability of the open porous network to provide continuous liquid replenishment dominated.

By contrast, the open pores on the Cu surface sustained both the liquid supply and BHTC and enabled a higher CHF.

When a porous structure is used to enhance pool boiling heat transfer, sufficient liquid supply through capillary wicking and enhancement of the nucleation site density provided by the pore structures are the primary mechanisms. However, efficient vapor release is essential to prevent dryout in the porous structure, because a greater thickness increases the vapor escape resistance. This could potentially lead to dryout inside the porous structure. Hence, thin microporous surfaces (Cu-1L and CuO-1L) were fabricated with the porous layer optimized to the minimum thickness, and their boiling heat transfer performance was subsequently examined.

Figure 16 shows the bubble behavior of Cu-1L and SiO_2 at similar heat flux levels (q_s = 650–700 kW/m^2). The BHTC of Cu-1L was enhanced by 471%, while the wall superheat was 15.0 °C lower than that of SiO_2. This improvement is attributed to the bubble dynamics. Small bubbles departed more frequently and rapidly than large bubbles because of their shorter growth times. Moreover, these bubbles transferred more heat generated from the surface owing to the rising action of numerous bubbles, leading to enhanced liquid mixing. Simultaneously, the thin microporous structure maintained sufficient liquid replenishment at the surface. This analysis indicates that tiny bubbles, balanced liquid replenishment, and vapor removal resistance are essential in boiling heat transfer enhancement and in single-layer microporous structures.

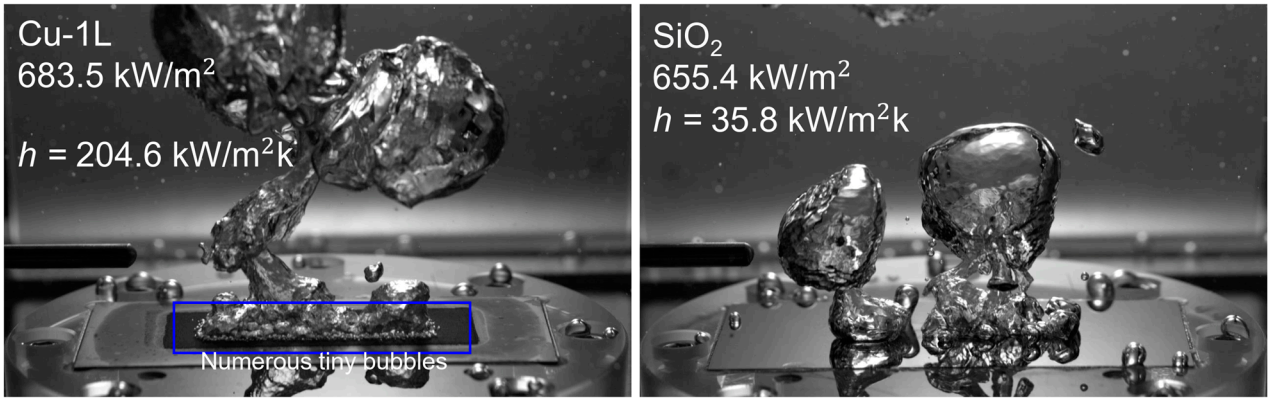


Figure 16. Comparison of the bubble behavior on Cu-1L and SiO_2 at q_s = 650–700 kW/m^2.

The role of the pillar structures was further examined by fabricating microporous substrates with millimeter-scale pillars, thereby combining micrometer-scale pores with millimeter-scale features that represented the near- and far-field regions of the boiling surface. Compared with their single-layer counterparts, the CHF values of Cu-Pil and CuO-Pil were enhanced by factors of 1.9 and 1.6, respectively, owing to the distinctive architecture of the Cu-Pil substrate. Figures 17 and 18 present the bubble dynamics at high heat fluxes (q_s > 600 kW/m^2). On the 1L surface, tiny bubbles continuously nucleate and rapidly coalesce with neighboring bubbles, making it difficult to identify when the surface was rewetted by the liquid.

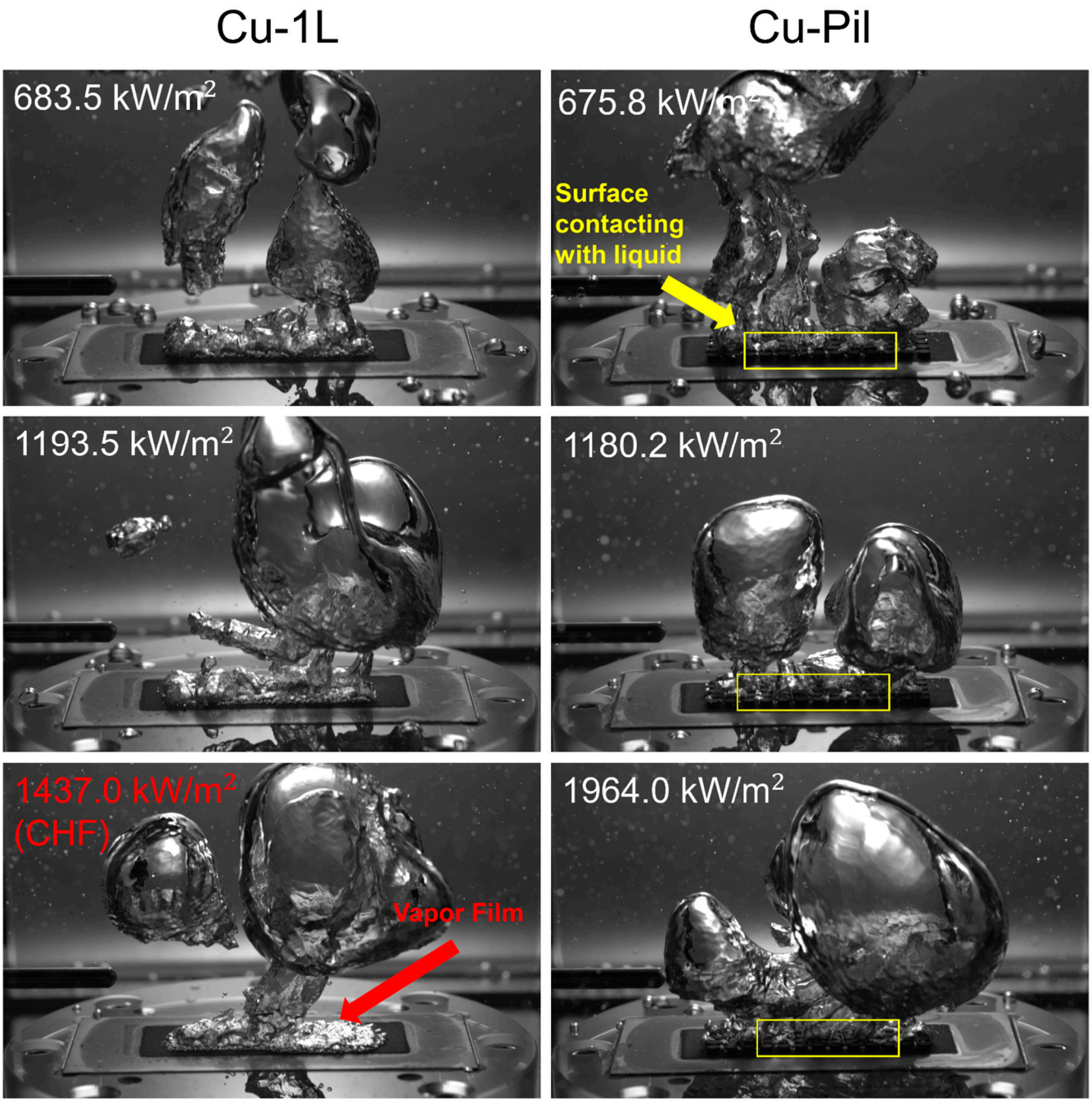


Figure 17. Comparison between the bubble dynamics of Cu-1L and Cu-Pil at relatively high surface heat flux.

By contrast, on the pillar surfaces, bubbles form only from the microporous base layer and rise between the pillars without interference, while the pillar tops remain cooler and do not serve as nucleation sites. Instead, these regions continuously absorb liquid through capillary wicking and gravity. Consequently, the spatial separation of the liquid and vapor pathways enables stable fluid flow, which enhances both the BHTC and CHF on the pillar surfaces.

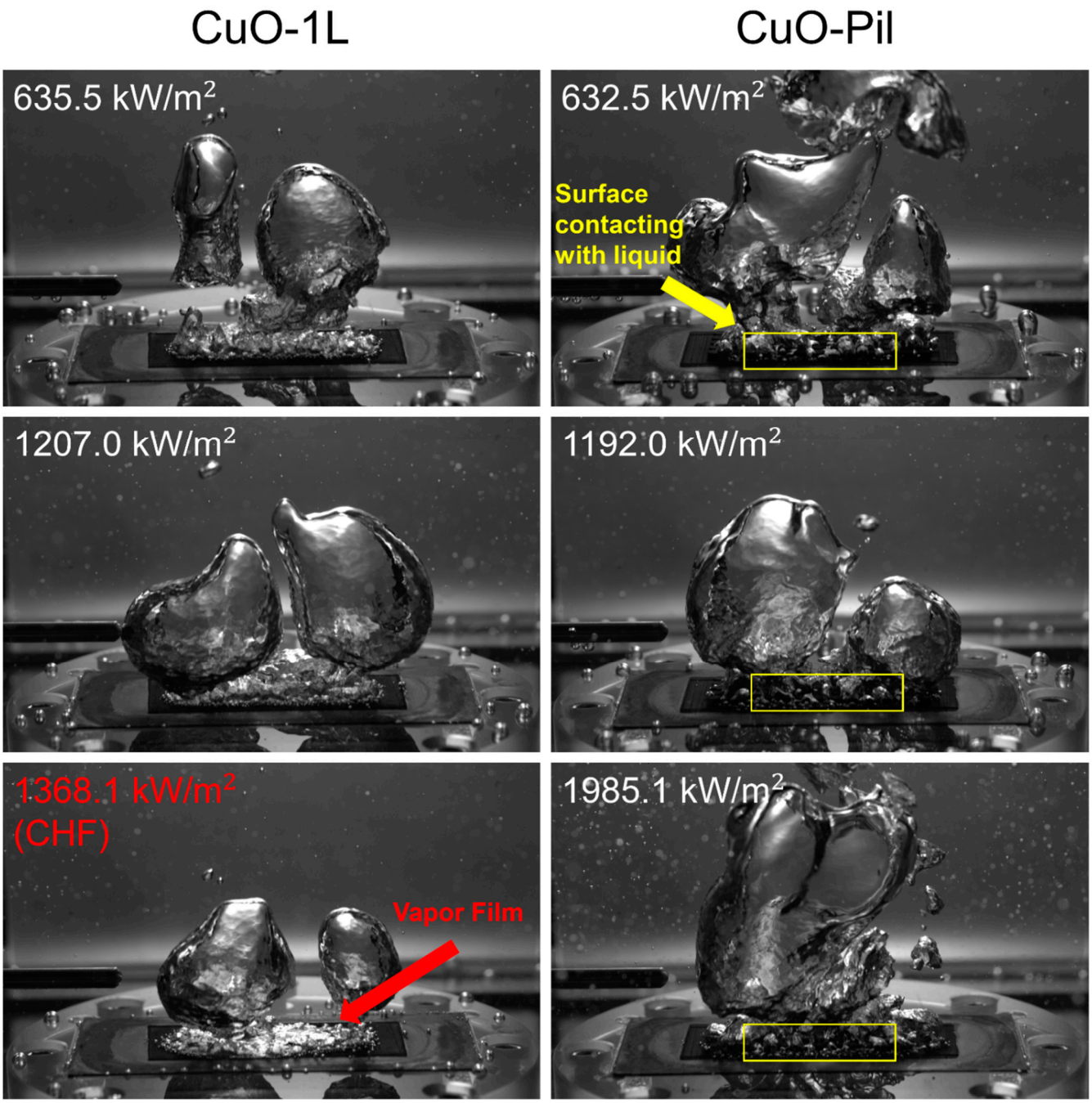


Figure 18. Comparison between the bubble dynamics of CuO-1L and CuO-Pil at relatively high surface heat flux.

Figure 19 shows the processed image sequences of the bubble behavior on the pillar structures, highlighting the vapor bubble growth (blue) and liquid-wetted regions (red). The arrows denote the representative regions of bubble generation and liquid contact, clearly indicating where vapor formation and surface wetting occur simultaneously in the pillar structures.

The schematic mechanism shown in Figure 20 summarizes this observation and illustrates the liquid–vapor pathway separation enabled by the microporous pillar structure. The liquid penetrates downward through the porous network (solid arrows), while the vapor simultaneously escapes upward through the open channels between the pillars (dashed arrows). This conceptual mechanism highlights how spatial separation of the

liquid and vapor flows minimizes the flow interference, suppresses the formation of dry spots, and sustains stable boiling heat transfer under high heat flux conditions.

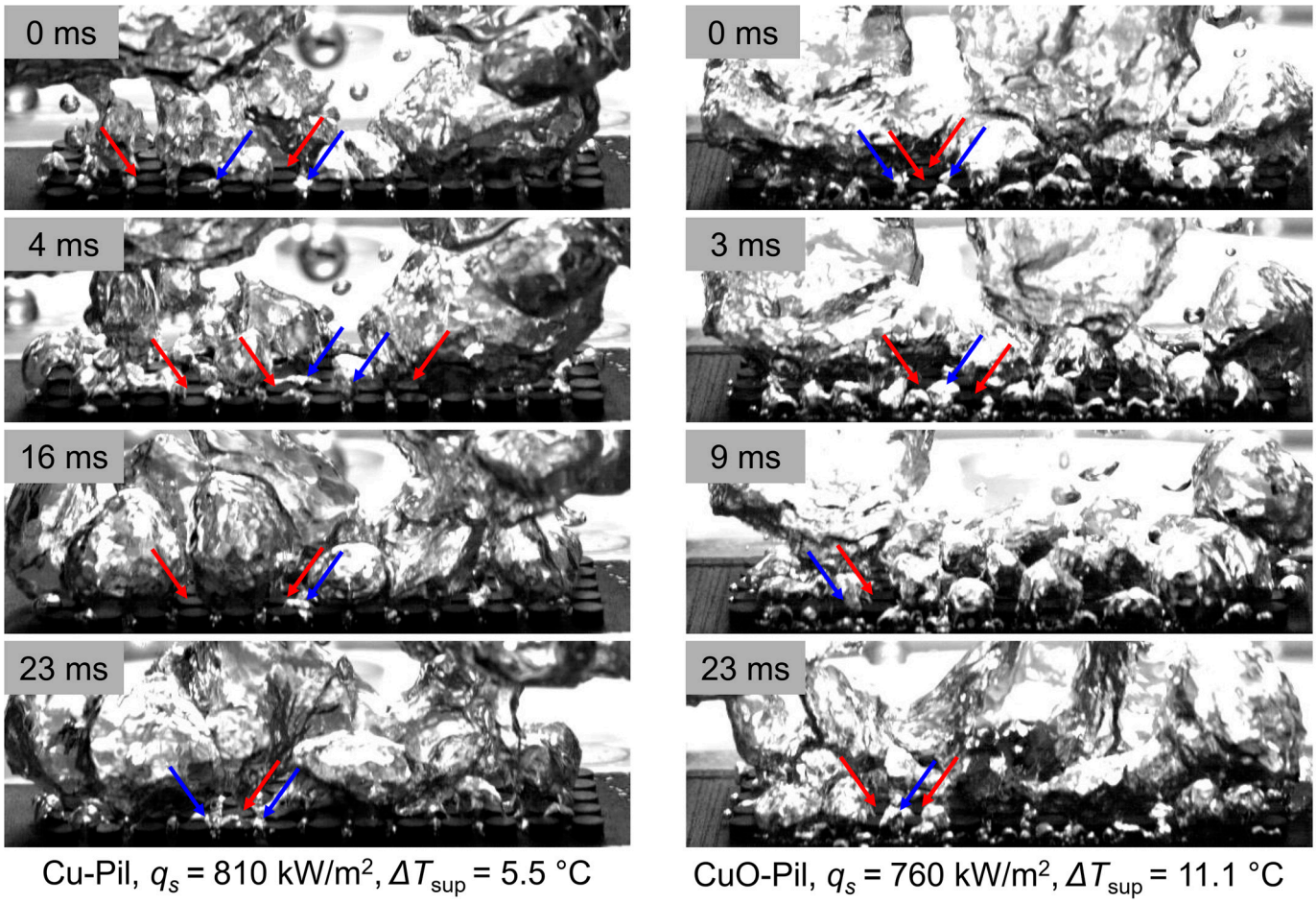


Figure 19. Observation of the pathway separation of vapor (blue arrows) growth and liquid (red arrows) contacting surface.

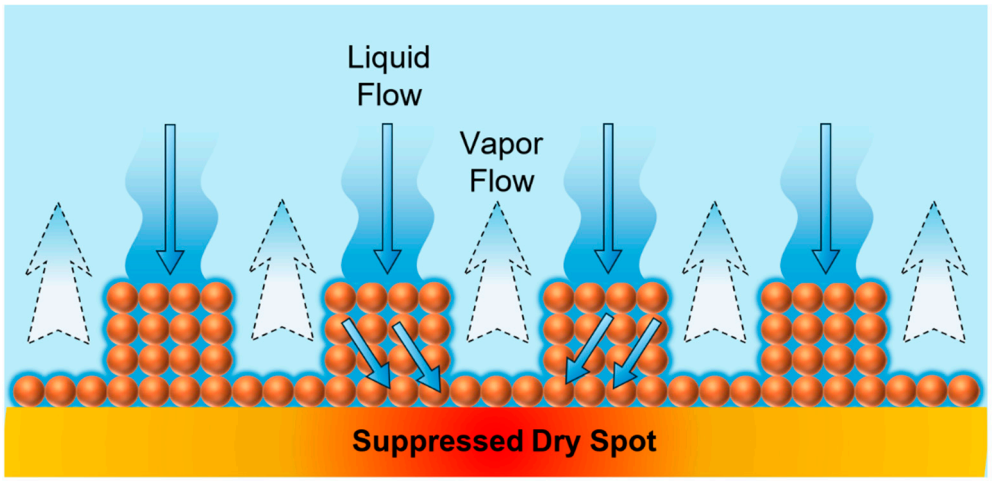


Figure 20. Schematic of the liquid and vapor path separation on the pillar structure boiling surface.

The CuO-Pil surface exhibited a distinctive surface temperature behavior. At relatively low heat fluxes, the CuO surfaces exhibited higher BHTC than the Cu surfaces. However, at higher heat fluxes (q_s > 516 kW/m^2), both the BHTC and CHF values of the CuO surfaces were lower than those of the Cu surfaces. The underlying mechanism responsible for the

reduced BHTC at elevated heat fluxes may be explained as follows: Enhancement of the boiling heat transfer at high heat flux conditions requires rapid rewetting of dry spots and the prompt detachment of merged vapor bubbles, which involves continuous liquid replenishment and efficient vapor removal.

As shown in Figure 21, the expansion of the merged bubbles on the CuO-Pil surface was significantly longer than that on the Cu-Pil because of the structural differences observed in the SEM images (Figure 14b). The open pore network of the Cu-Pil surface facilitated rapid liquid replenishment, which shortened the expansion time of the merged bubbles.

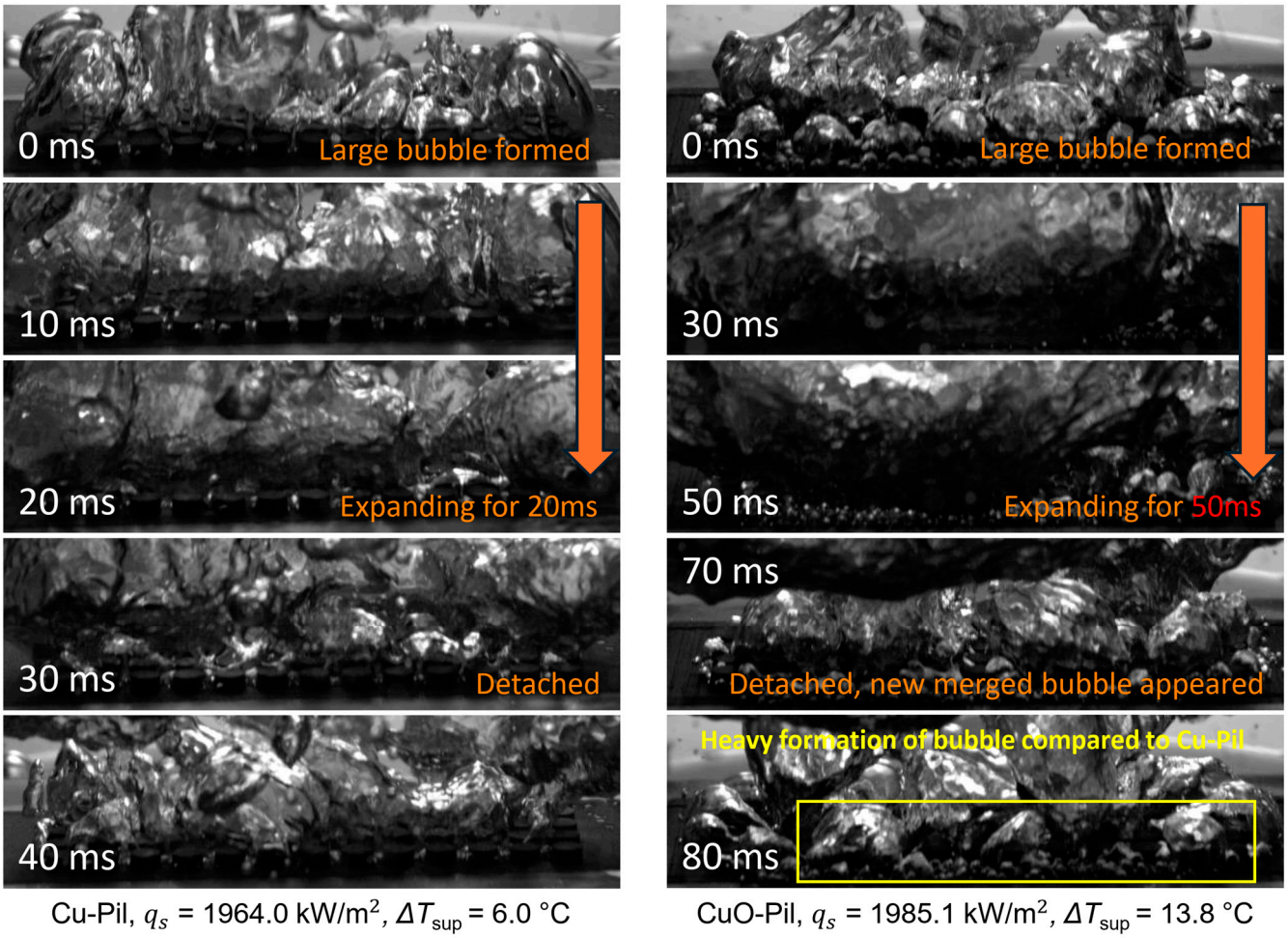


Figure 21. Expansion and detachment behaviors of large bubbles on Cu-Pil and CuO-Pil, at high heat flux.

By contrast, the closed-end pore morphology of the CuO-Pil surface limited the liquid supply at high heat fluxes, whereas the higher density of nucleation sites promoted the formation of larger merged bubbles with prolonged lifetimes. Consequently, excessive bubble growth hindered effective rewetting, leading to persistent dry regions, elevated wall superheating, and a lower CHF compared with those of Cu-Pil.

However, CuO-Pil exhibited a unique temperature peak and recovery phenomenon. Figure 22 shows the changes in the wall superheat and surface heat flux at each temperature peak. During these temperature peaks, the wall superheat exhibits two-stage behavior with increasing heat flux. When the Pt heater power increases, the boiling surface temperature increases rapidly within a few seconds, suggesting the apparent formation of irreversible dry spots.

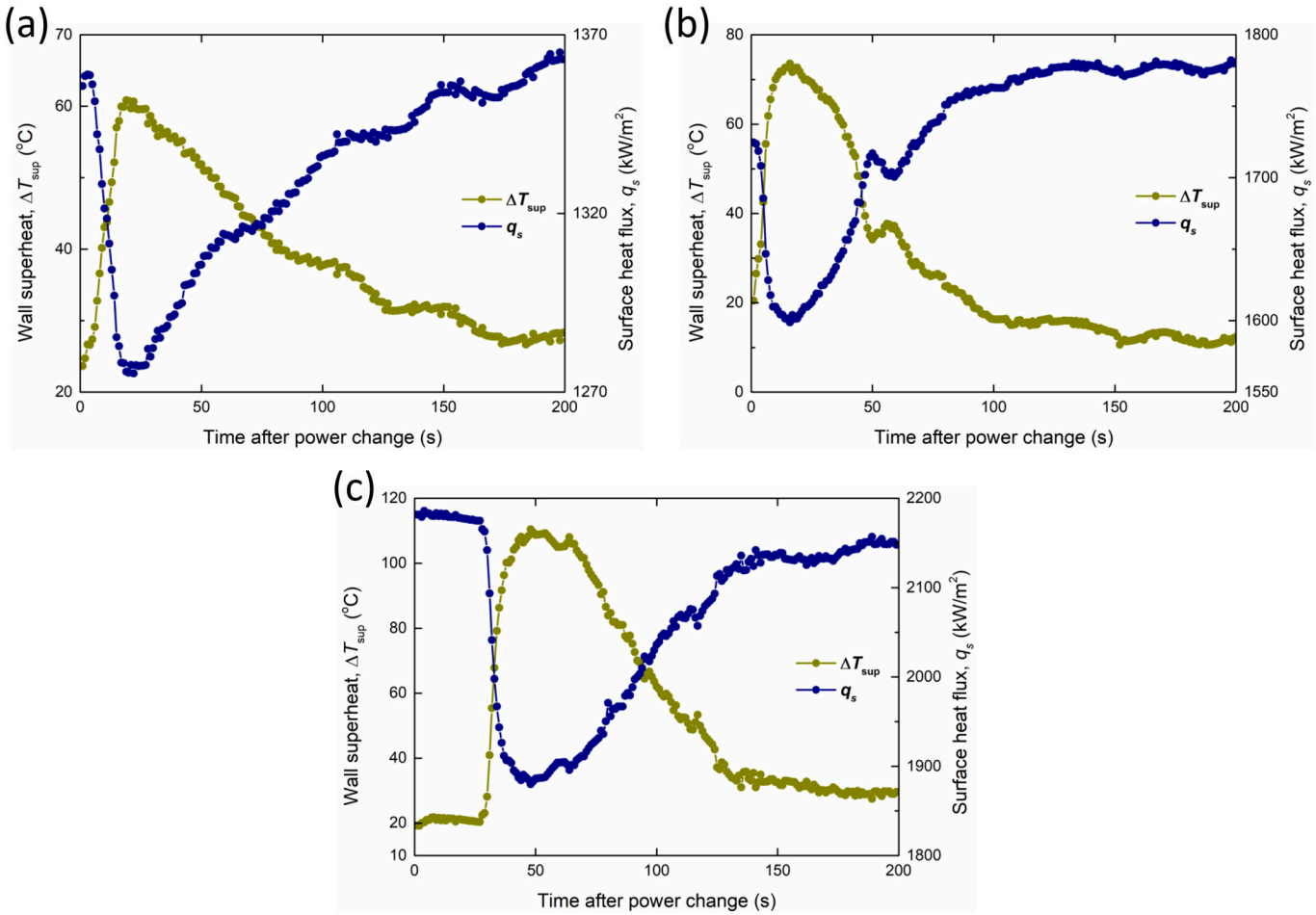


Figure 22. Changes in the wall superheat and surface heat flux at each temperature peak, with heat flux values finally converging to (**a**) 1373 kW/m^2, (**b**) 1785 kW/m^2, and (**c**) 2138 kW/m^2 in CuO-Pil.

Nevertheless, the boiling surface does not undergo irreversible burnout. Instead, the temperature gradually decreases over several tens of seconds and returns to the nucleate boiling regime under stable conditions, with the transient surface temperature peaking at 210 °C. This recovery was enabled by the strong capillary wicking of the nanostructured porous layer, which continuously supplied liquid to the overheated regions owing to its strong wettability.

Consequently, the temporal and localized dry spots were rewetted before they developed into a fully established CHF condition. Such transient overheating followed by recovery has not been reported in conventional pool boiling experiments and highlights the unique role of superhydrophilicity and enhanced liquid supply in stabilizing the boiling process on the CuO-Pil surface. The temperature peak phenomenon of the CuO-Pil surface and the CHF of the CuO-1L surface were attained at approximately the same heat flux. Thus, the additional liquid supply from the superhydrophilicity of the nanostructured pillars was sufficient to rewet the vapor films, which would otherwise trigger the CHF on the CuO-1L surface, thereby extending the stable boiling regime.

Additionally, the distinctive temperature behavior of CuO-Pil influenced the CHF conditions. Figure 23a,b show the wall superheat behavior when the CHF occurred in CuO-1L and CuO-Pil, respectively. CuO-1L exhibits a typical CHF phenomenon in which the surface temperature increases rapidly and abruptly owing to the formation of irreversible dry spots. However, in CuO-Pil, the temperature gradually increases in a step-like manner despite reaching the CHF level, as shown in Figure 23c. Finally, after more than 200 s of increasing tendency, the temperature increases rapidly.

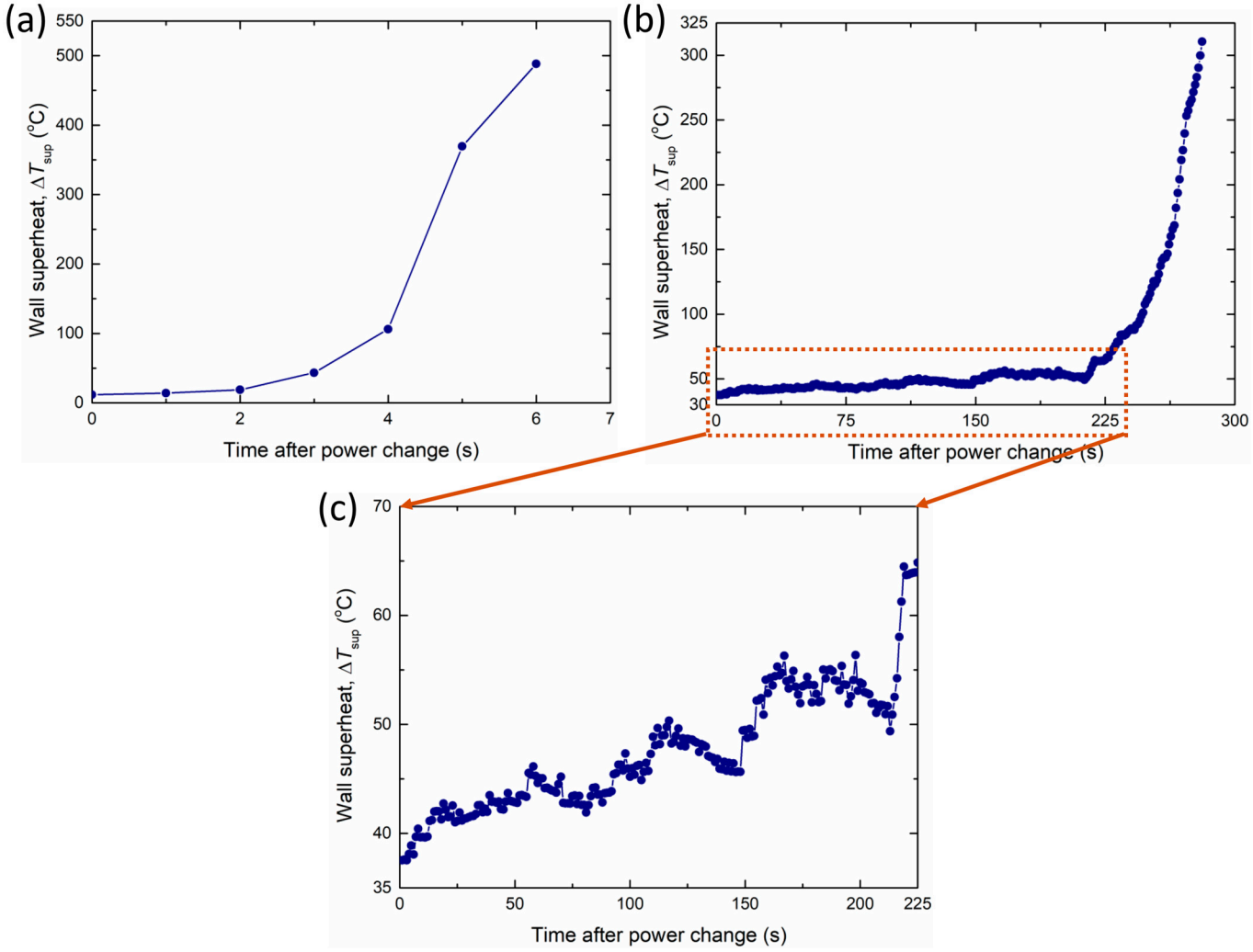


Figure 23. Sequential wall superheat behavior at the CHF in (**a**) CuO-1L (**b**), (**c**) CuO-Pil.

However, during the rapid rise in temperature, the maximum temperature rise rate of the CuO-Pil surface was only 14.9 °C/s, whereas that of CuO-1L was 263.1 °C/s. The synergy between the superhydrophilicity of the nanostructure and the pillar structure, which was achieved through the integrated micro/nanostructured design of the CuO-Pil surface, resulted in this unique phenomenon.

Compared with nanofluid-based approaches, which typically show CHF enhancement but mixed BHTC trends depending on particle loading and deposition history, the present additive-free, surface modification achieves stable boiling improvement through geometric liquid–vapor pathway separation and capillary wicking. While nanofluids rely on nanoparticle deposition and evolving surface wettability, this method provides a fixed and repeatable micro/nanostructure for sustained liquid supply and vapor removal.

Nanofluids may be attractive for retrofit applications where surface modification is impractical, but they often require careful control of coolant purity and long-term stability. In contrast, the multiscale porous structure ensures reliable operation under additive-free conditions, making it suitable for closed-loop or reliability-critical cooling systems.

4. Conclusions

In this study, five boiling substrates (SiO_2, Cu-1L, Cu-Pil, CuO-1L, and CuO-Pil) were fabricated using metal powder sintering and thermal oxidation. The boiling heat transfer performance was evaluated under saturated pool boiling conditions. By comparing the

BHTC and CHF values, the underlying mechanisms of boiling heat transfer enhancement were identified and supported by high-speed visualization. A unique phenomenon, which was named "temperature peak and recovery," was observed. These results highlight that surface modification, additive-free designs offer a stable alternative to nanofluid-based enhancement, particularly for reliability-critical systems. The main findings of this study are summarized as follows:

1. Under low heat flux, both the Cu and CuO surfaces exhibited similarly enhanced boiling behaviors. However, the CuO surfaces exhibited a higher BHTC owing to the distinct closed-end pore morphology of the CuO surfaces, which provided a higher density of active nucleation sites and produced smaller bubbles. These promoted more frequent bubble nucleation and departure, shorter bubble lifetimes, and faster surface rewetting, thereby sustaining a more efficient heat transfer in the low heat flux regime.
2. The enhancement of boiling heat transfer by a thin microporous layer was attributed to the reduced vapor escape resistance achieved by sintering the Cu particles into an almost single layer. At $q_s \approx 670$ kW/m^2, the BHTC of Cu-1L was enhanced by 471%, while the wall superheat was 15 °C lower than that of SiO_2. This improvement was further evidenced by the rapid generation of numerous tiny bubbles on the microporous surface, which were absent on SiO_2. The higher bubble frequency associated with these small bubbles facilitated the superior performance of Cu-1L in terms of the boiling heat transfer and CHF.
3. The microporous pillar structure strongly influenced both the near- and far-field regions of the boiling surface. Thus, the Cu-Pil and CuO-Pil surfaces increased the CHF by factors of 1.9 and 1.6 compared with those of the Cu-1L and CuO-1L surfaces, respectively. The dominant enhancement mechanism at high heat fluxes was the distinct separation of the liquid and vapor pathways. The pillar tops served as the liquid supply channels, whereas the bottom layer between the pillars served as a vapor escape route. This liquid–vapor path separation minimized flow interference and stabilized boiling, as supported by high-speed visualization showing continuous liquid contact on the pillar tops.
4. At high heat flux, the CuO-Pil surfaces exhibited a reduced BHTC and elevated wall superheat owing to delayed vapor detachment and severe bubble expansion arising from their high nucleation site density and closed-end pore morphology. Moreover, the CuO-Pil surface exhibited a unique "temperature peak and recovery" phenomenon, where temporal dry spots were rewetted by strong capillary wicking and liquid–vapor pathway separation from superhydrophilic micro/nanostructured design, thereby preventing irreversible burnout. Even near CHF, the temperature rise rate of the CuO-Pil surface was considerably slower (14.9 °C/s) than that of CuO-1L (263.1 °C/s), demonstrating that the integrated micro/nanostructured design extended the stable boiling regime and improved CHF tolerance.

Author Contributions: Conceptualization, D.-W.J. and D.E.K.; Methodology, D.J.L., Y.J.Y. and D.E.K.; Investigation, D.J.L., D.-W.J. and D.E.K.; Data curation, D.E.K.; Writing—original draft, D.J.L.; Writing—review & editing, Y.J.Y., D.-W.J. and D.E.K.; Funding acquisition, D.E.K. All authors have read and agreed to the published version of the manuscript.

Funding: This work was supported by the Innovative Small Modular Reactor Development Agency grant funded by the Korea Government (MSIT) (No. RS-2024-00408520). This research was supported by the Chung-Ang University Research Scholarship Grants in 2025.

Institutional Review Board Statement: Not applicable.

Informed Consent Statement: Not applicable.

Data Availability Statement: The original contributions presented in this study are included in the article. Further inquiries can be directed to the corresponding authors.

Conflicts of Interest: The authors declare no conflict of interest.

References

1. Jiang, W.; Lyu, P.; Liu, X.; Rao, Z. Temperature equalization strategy in immersion flow boiling battery thermal management: Optimization of flow regime in boiling heat transfer. *Appl. Therm. Eng.* **2025**, *267*, 125825. [CrossRef]
2. Ebrahim, S.A.; Pradeep, E.; Ahmed, M. Role of sea salt deposition on the advances in pool boiling heat transfer in nuclear reactors. *Appl. Therm. Eng.* **2022**, *217*, 119146. [CrossRef]
3. Huang, T.C.; Pan, C. Pool boiling in seawater, NaCl solution and de-ionized water. *Nucl. Eng. Des.* **2019**, *344*, 46–53. [CrossRef]
4. Sun, Y.; Li, H.; Chen, J.; Wu, C.; Tang, H.; Zhang, S.; Tang, Y. Hierarchical sintered porous surfaces with enhanced pool boiling heat transfer performance for high-power cooling applications. *Appl. Therm. Eng.* **2024**, *249*, 123368. [CrossRef]
5. Xiong, H.; Li, X.; Chen, C.; Xin, G.; Li, J.; Chen, Y. Experimental study on the heat transfer performance of a gravity-assisted separated heat pipe for high-power chip cooling. *Energy* **2025**, *332*, 136066. [CrossRef]
6. Kim, D.E.; Oh, J.S. Local phase and thermal behaviors in pool boiling on different wettability surfaces. *Exp. Therm. Fluid Sci.* **2022**, *139*, 110728. [CrossRef]
7. Kim, H.; Kim, D.E. Effects of surface wettability on pool boiling process: Dynamic and thermal behaviors of dry spots and relevant critical heat flux triggering mechanism. *Int. J. Heat Mass Transf.* **2021**, *180*, 121762. [CrossRef]
8. Kim, D.E.; Park, J. Experimental study of critical heat flux in pool boiling using visible-ray optics. *Int. J. Heat Mass Transf.* **2021**, *169*, 120937. [CrossRef]
9. Sun, X.; Li, Q.; Liu, B.; Chang, H. Composite microstructured surface with micro-cavities and micro-ditches on micro-pin-fins for enhancing pool boiling heat transfer. *Appl. Therm. Eng.* **2024**, *252*, 123713. [CrossRef]
10. Wang, X.; Fadda, D.; Godinez, J.; Lee, J.; You, S.M. Effect of wettability on pool boiling heat transfer with copper microporous coated surface. *Int. J. Heat Mass Transf.* **2022**, *194*, 123059. [CrossRef]
11. Wang, D.; Lin, T.; Quan, X. Enhanced liquid replenishment for pool boiling heat transfer and its CHF mechanism on patterned freeze-casted surfaces. *Exp. Therm. Fluid Sci.* **2024**, *150*, 111035. [CrossRef]
12. Park, S.C.; Kim, J.M.; Kim, T.; Kim, M.H.; Ahn, H.S. Boiling characteristics on a serpentine-like geometry thin-film platinum heater under pool boiling. *Int. J. Heat Mass Transf.* **2016**, *95*, 214–223. [CrossRef]
13. Lv, Z.; An, Y.; Huang, C. Enhanced pool boiling heat transfer by adding metalized diamond in copper porous materials. *Appl. Therm. Eng.* **2023**, *226*, 120288. [CrossRef]
14. Zhang, K.; Bai, L.; Yao, G.; Wen, D. Influence of pore size distribution on pool boiling heat transfer in porous artery structure. *Int. J. Heat Mass Transf.* **2023**, *209*, 124116. [CrossRef]
15. Kumar, R.; Premachandran, B. Enhancement of pool boiling performance through an asymmetric dual V-groove microchannel structured surface. *Int. J. Heat Mass Transf.* **2024**, *221*, 125096. [CrossRef]
16. Liu, H.; Wang, J.; Gu, Z.; Fei, X.; Zhang, L. Enhancement of pool boiling heat transfer using 3D-printed groove structure. *Int. J. Heat Mass Transf.* **2022**, *183*, 122155. [CrossRef]
17. Tang, Y.-Q.; Hu, X.-J.; Wang, Z.-J.; Sun, C.-H.; Fang, W.-Z.; Tao, W.-Q. Enhanced pool boiling of Novec-7100 using nano/micro structured surfaces. *Int. J. Heat Mass Transf.* **2025**, *250*, 127320. [CrossRef]
18. Gouda, R.K.; Pathak, M.; Khan, M.K. Pool boiling heat transfer enhancement with segmented finned microchannels structured surface. *Int. J. Heat Mass Transf.* **2018**, *127*, 39–50. [CrossRef]
19. Zhang, S.; Tang, Y.; Zeng, J.; Yuan, W.; Chen, J.; Chen, C. Pool boiling heat transfer enhancement by porous interconnected microchannel nets at different liquid subcooling. *Appl. Therm. Eng.* **2016**, *93*, 1135–1144. [CrossRef]
20. Hu, H.; Zhao, Y.; Lai, Z.; Hu, C. Influence of surface wettability on pool boiling heat transfer on metal foam covers. *Int. J. Therm. Sci.* **2021**, *168*, 107069. [CrossRef]
21. Lim, H.; Doh, S.-Y.; Choi, J.; Moc, J.; You, S.M.; Lee, J. Pool boiling heat transfer enhancement using the micro-thick metallic foam surface in saturated water. *Int. Commun. Heat Mass Transf.* **2024**, *152*, 107310. [CrossRef]
22. Sharifzadeh, A.M.; Moghadasi, H.; Shakeri, H.; Saffari, H. Influence of bubble departure control on nucleate pool boiling heat transfer of electrodeposited copper foam: Experiments and correlation. *Int. Commun. Heat Mass Transf.* **2022**, *138*, 106381. [CrossRef]
23. Kim, H.; Jung, E.; Ryu, C.; Lee, H.; In, J.B. Nanosecond laser structuring for enhanced pool boiling performance of SiC surfaces. *Appl. Surf. Sci.* **2024**, *675*, 160977. [CrossRef]
24. Lee, S.; Kim, Y.; Ki, H.; Lee, J. Femtosecond laser-treated copper sintering surface to enhance pool boiling heat transfer. *Int. Commun. Heat Mass Transf.* **2024**, *152*, 107270. [CrossRef]

25. Lou, D.; Yang, D.; Dong, C.; Chen, C.; Jiang, H.; Li, Q.; Cheng, J.; Lu, G.; Liu, D. Enhancement of pool boiling heat transfer by laser texture-deposition on copper surface. *Appl. Surf. Sci.* **2024**, *661*, 160015. [CrossRef]
26. Wong, K.K.; Leong, K.C. Saturated pool boiling enhancement using porous lattice structures produced by Selective Laser Melting. *Int. J. Heat Mass Transf.* **2018**, *121*, 46–63. [CrossRef]
27. Kalita, S.; Sen, D.; Sen, P.; Das, S.; Saha, B.B. Pool boiling heat transfer enhancement and bubble visualization on a microporous copper over CuO filmed surface through combination of chemical etching and electrochemical deposition. *Int. Commun. Heat Mass Transf.* **2023**, *144*, 106740. [CrossRef]
28. Mousa, M.H.; Roni, M.R.H.; Rao, R.; Ganesan, V.; Khodakarami, S.; Yang, C.-M.; Rabbi, K.F.; Upot, N.V.; Nawaz, K.; Miljkovic, N. Water flow boiling heat transfer and pressure drop in smooth, etched, and herringbone aluminum tubes. *Appl. Therm. Eng.* **2024**, *257*, 124426. [CrossRef]
29. Kim, H.; Park, Y.; Kim, H.; Lee, C.; Jerng, D.W.; Kim, D.E. Critical heat flux enhancement by single-layered metal wire mesh with micro and nano-sized pore structures. *Int. J. Heat Mass Transf.* **2017**, *115*, 439–449. [CrossRef]
30. Dang, C.; Min, R.; Pan, L.; Yin, L.; Zhang, Z.; Hu, Y. Saturated pool boiling heat transfer enhancement of R245fa based on the surface covered by sintered copper powder with and without nanostructure. *Int. J. Therm. Sci.* **2023**, *187*, 108183. [CrossRef]
31. Jaikumar, A.; Kandlikar, S.G. Enhanced pool boiling heat transfer mechanisms for selectively sintered open microchannels. *Int. J. Heat Mass Transf.* **2015**, *88*, 652–661. [CrossRef]
32. Jun, S.; Kim, J.; Son, D.; Kim, H.Y.; You, S.M. Enhancement of pool boiling heat transfer in water using sintered copper microporous coatings. *Nucl. Eng. Technol.* **2016**, *48*, 932–940. [CrossRef]
33. Wang, X.; Wan, Z. Heat transfer performance of a heat pipe with sintered stainless-steel fiber wick. *Case Stud. Therm. Eng.* **2023**, *45*, 103016. [CrossRef]
34. Zhang, D.; Mao, J.; Qu, J.; Lei, Q.; Li, C.; Chen, Y. Characterizing effect of particle size on flow boiling in sintered porous-microchannels. *Appl. Therm. Eng.* **2023**, *229*, 120571. [CrossRef]
35. Lin, Y.; Wang, T.H.; Wang, C.-C. Pool boiling performance for GaldenR HT 55 subject to smooth, pin fin, and sintered pin fin heat sink. *Int. J. Therm. Sci.* **2024**, *202*, 109090. [CrossRef]
36. Lee, S.; Kim, Y.; Ki, H.; Lee, J. Critical heat flux in pool boiling on femtosecond laser-irradiated copper powder-sintered surfaces. *Therm. Sci. Eng. Prog.* **2025**, *60*, 103421. [CrossRef]
37. Ranjan, A.; Ahmad, I.; Gouda, R.K.; Pathak, M.; Khan, M.K. Enhancement of critical heat flux (CHF) in pool boiling with anodized copper surfaces. *Int. J. Therm. Sci.* **2022**, *172*, 107338. [CrossRef]
38. Shim, D.I.; Yun, M.; Kim, Y.-H.; Lee, D.; Cho, H.H. 3D-Printed vapor guiding structures for enhanced pool boiling heat transfer. *Int. J. Mech. Sci.* **2025**, *286*, 109865. [CrossRef]
39. Chen, Y.; Li, P.; Zou, Q.; Liu, X.; Yang, R. Enhancing pool boiling with separated liquid-vapor pathways on perforated micromesh surface. *Int. J. Heat Mass Transf.* **2025**, *244*, 126949. [CrossRef]
40. Jin, L.W.; Leong, K.C.; Pranoto, I. Saturated pool boiling heat transfer from highly conductive graphite foams. *Appl. Therm. Eng.* **2011**, *31*, 2685–2693. [CrossRef]
41. Pranoto, I.; Leong, K.C.; Jin, L.W. The role of graphite foam pore structure on saturated pool boiling enhancement. *Appl. Therm. Eng.* **2012**, *42*, 163–172. [CrossRef]
42. Liu, B.; Yang, X.; Jie, Z.; Wei, J.; Li, Q. Enhanced pool boiling on micro-nano composited surfaces with nanostructures on micro-pin-fins. *Int. J. Heat Mass Transf.* **2022**, *190*, 122812. [CrossRef]
43. Jiang, X.; Shah, S.W.A.; Chen, G.; Xie, S. Extraordinary boiling enhancement by hybrid dividing zonesS of micro-nano structures. *Int. Commun. Heat Mass Transf.* **2024**, *153*, 107345. [CrossRef]
44. Ahn, H.S.; Lee, C.; Kim, J.; Kim, M.H. The effect of capillary wicking action of micro/nano structures on pool boiling critical heat flux. *Int. J. Heat Mass Transf.* **2012**, *55*, 89–92. [CrossRef]
45. Milanova, D.; Kumar, R. Heat transfer behavior of silica nanoparticles in pool boiling experiment. *J. Heat Transf.* **2008**, *130*, 042401. [CrossRef]
46. Raveshi, M.R.; Keshavarz, A.; Mojarrad, M.S.; Amiri, S. Experimental investigation of pool boiling heat transfer enhancement of alumina-water-ethylene glycol nanofluids. *Exp. Therm. Fluid Sci.* **2013**, *44*, 805–814. [CrossRef]
47. Khan, A.; Muhammad, A.F. A comprehensive review on pool boiling heat transfer using nanofluids. *Therm. Sci.* **2019**, *23*, 3209–3237. [CrossRef]
48. Du, J.; Wang, Y.; Yang, W.; Wang, J.; Cao, Z.; Sundén, B. Effect of nanoparticle concentration and surfactants on nanofluid pool boiling. *Int. J. Heat Mass Transf.* **2024**, *221*, 125080. [CrossRef]
49. Bregar, T.; Hadžić, A.; Robinson, J.; Askounis, A.; Zupančič, M.; Golobič, I. Additively manufactured copper surfaces with porous microfeatures for enhanced pool boiling performance. *Int. J. Therm. Sci.* **2026**, *220*, 110325. [CrossRef]
50. Liu, X.; Liu, B.; Li, Q.; Li, W. Enhanced pool boiling heat transfer on multilayer-gradient-porosity pillar-structured surfaces. *Int. J. Heat Mass Transf.* **2026**, *255*, 127747. [CrossRef]

51. Guan, S.Y.; Zhang, Z.H.; Wu, R.; Zhao, C.Y. Boiling heat transfer via micro–nano composite gradient and grooved porous structures: Liquid film and vapor dynamics insights. *Int. J. Heat Mass Transf.* **2026**, *254*, 127655. [CrossRef]
52. Kumar, R.; Premachandran, B. Pool boiling performance enhancement using a scalable thermally sprayed porous copper coating. *Int. J. Heat Mass Transf.* **2025**, *247*, 127199. [CrossRef]
53. Balsamy-Kamaraj, A.; Hasan, M.M.; Merugu, S.; Gupta, A. Comparison of 3D-printed copper surfaces for enhanced pool boiling heat transfer. *Manuf. Lett.* **2025**, *44*, 1649–1656. [CrossRef]
54. Lee, D.J.; Yang, Y.J.; Kim, D.E. Boiling performance enhancement and self-recovery of nucleate boiling regime on micro- and nanostructured porous surfaces. *Int. J. Heat Mass Transf.* **2025**, *238*, 126516. [CrossRef]
55. Liu, D.; Jiao, R.; Sun, C.; Wang, Y. Effects of substrates on the performance of Pt thin-film resistance temperature detectors. *Coatings* **2024**, *14*, 969. [CrossRef]
56. Wang, H.; Liu, Z.; Wang, B.; Kong, M.; Xu, D.; Gao, L.; Li, Q.; Zhao, Z.; Lu, W.; Zhao, X.; et al. Stability enhancement of the platinum thin-film temperature detector up to 1400 °C by printing Al_2O_3 protective layer. *IEEE Sensors J.* **2024**, *24*, 17433–17440. [CrossRef]
57. Yamasue, E.; Susa, M.; Fukuyama, H.; Nagata, K. Thermal conductivities of silicon and Germanium in solid and liquid states measured by non-stationary hot wire method with silica coated probe. *J. Cryst. Growth* **2002**, *234*, 121–131. [CrossRef]
58. Love, C.J.; Smith, J.D.; Cui, Y.; Varanasi, K.K. Size-dependent thermal oxidation of copper: Single-step synthesis of hierarchical nanostructures. *Nanoscale* **2011**, *3*, 4972. [CrossRef]
59. Kline, S.J. Describing uncertainties in single-sample experiments. *Mech. Eng.* **1953**, *75*, 3–8.
60. Moffat, R.J. Describing the uncertainties in experimental results. *Exp. Therm. Fluid Sci.* **1988**, *1*, 3–17. [CrossRef]
61. Jaikumar, A.; Kandlikar, S.G. Pool boiling inversion through bubble induced macroconvection. *Appl. Phys. Lett.* **2017**, *110*, 094107. [CrossRef]
62. Zuber, N. Hydrodynamic Aspects of Boiling Heat Transfer. Ph.D. Thesis, University of California, Los Angeles, CA, USA, 1959.

Disclaimer/Publisher's Note: The statements, opinions and data contained in all publications are solely those of the individual author(s) and contributor(s) and not of MDPI and/or the editor(s). MDPI and/or the editor(s) disclaim responsibility for any injury to people or property resulting from any ideas, methods, instructions or products referred to in the content.